AD-A199 532

TECHNICAL REPORT BRL-TR-2935

BRL

1938 – Serving the Army for Fifty Years – 1988

AXISYMMETRIC CALCULATIONS FOR THE LARGE BLAST/THERMAL SIMULATOR (LB/TS) SHOCK TUBE CONFIGURATION

DIXIE M. HISLEY
GREGORY A. MOLVIK

SEPTEMBER 1988

DTIC
SELECTED
OCT 1 4 1988
E

U.S. ARMY LABORATORY COMMAND

BALLISTIC RESEARCH LABORATORY

ABERDEEN PROVING GROUND, MARYLAND

88 1011 274

REPORT DOCUMENTATION PAGE		*Form Approved* *OMB No. 0704-0188*

1a. REPORT SECURITY CLASSIFICATION Unclassified	1b. RESTRICTIVE MARKINGS	
2a. SECURITY CLASSIFICATION AUTHORITY	3. DISTRIBUTION / AVAILABILITY OF REPORT	
2b. DECLASSIFICATION / DOWNGRADING SCHEDULE		

4. PERFORMING ORGANIZATION REPORT NUMBER(S) BRL-TR-2935	5. MONITORING ORGANIZATION REPORT NUMBER(S)

6a. NAME OF PERFORMING ORGANIZATION Ballistic Research Laboratory	6b. OFFICE SYMBOL *(If applicable)* SLCBR-TB-B	7a. NAME OF MONITORING ORGANIZATION Harry Diamond Laboratories
6c. ADDRESS *(City, State, and ZIP Code)* Aberdeen Proving Ground, MD 21005-5066		7b. ADDRESS *(City, State, and ZIP Code)* Adelphi, MD 20783-1197

8a. NAME OF FUNDING / SPONSORING ORGANIZATION Harry Diamond Laboratories	8b. OFFICE SYMBOL *(If applicable)* SLCHD-TI	9. PROCUREMENT INSTRUMENT IDENTIFICATION NUMBER

8c. ADDRESS *(City, State, and ZIP Code)*	10. SOURCE OF FUNDING NUMBERS			
	PROGRAM ELEMENT NO.	PROJECT NO.1L162120 AH25	TASK NO. 44061- 801-63	WORK UNIT ACCESSION NO.
Adelphi, MD 20783-1197				

11. TITLE *(Include Security Classification)* Axisymmetric Calculations for the Large Blast/Thermal
Simulator (LB/TS) Shock Tube Configuration

12. PERSONAL AUTHOR(S)
Hisley, Dixie M., and Molvik, Gregory A

13a. TYPE OF REPORT Technical	13b. TIME COVERED FROM Jan 86 TO Sep 86	14. DATE OF REPORT *(Year, Month, Day)*	15. PAGE COUNT

16. SUPPLEMENTARY NOTATION

17.	COSATI CODES		18. SUBJECT TERMS *(Continue on reverse if necessary and identify by block number)*		
FIELD	GROUP	SUB-GROUP	Euler	Finite Volume	Nozzle Flow
20	04		Blast 2D Code	Large-Scale Blast Simulator	Upwind
01	01		Heated Driver	Total Variation Diminishing	

19. ABSTRACT *(Continue on reverse if necessary and identify by block number)*
Computational fluid dynamics (CFD) is a tool which predicts the gas dynamics of blast
problems of interest to the Army by solving a set of mathematical equations with a high-
speed digital computer. The governing equations for the blast problems presented here are
the two-dimensional unsteady Euler equations. The computations were performed on a Cray
XMP/48 supercomputer by discretizing the Euler equations with an upwind, Total Variation
Diminishing (TVD), finite volume, implicit scheme. Details of the scheme are presented in
the paper. The algorithm is used here to provide gas dynamic information for a candidate
large-scale blast simulator (LBS) concept.

existing is conducting

The Army has a growing need for nuclear blast survivability testing of tactical equipment.
In order to meet this need, the Army is conducting research into the design and operation
of a Large-scale Blast Thermal Simulator (LBTS), essentially a large multi-driver shock tube.
Experiments with heated and unheated driver gas have been performed in a single driver, 1/57

20. DISTRIBUTION / AVAILABILITY OF ABSTRACT ☐ UNCLASSIFIED/UNLIMITED ☒ SAME AS RPT ☐ DTIC USERS	21. ABSTRACT SECURITY CLASSIFICATION Unclassified	
22a. NAME OF RESPONSIBLE INDIVIDUAL Dixie M. Hisley	22b. TELEPHONE *(Include Area Code)* (301) 278-6027	22c. OFFICE SYMBOL SLCBR-TB-B

DD Form 1473, JUN 86 — *Previous editions are obsolete.* — SECURITY CLASSIFICATION OF THIS PAGE

19. ABSTRACT (Continued):

scale model of the LB/TS design concept but without the thermal simulation (LBS). One
dimensional calculations have been performed for the 1/57 scale LBS with useful results.
However, the one-dimensional calculations have had limited success for accurately
predicting the flow through the diverging portion of the LBS design because the flow in
this region is multi-dimensional. The flow is multi-dimensional due to the rapid and
large area change that exists in the diverging nozzle. The paper presents results
which demonstrate the nature of fluid physics in the 1/57 scale LBS.

DISPOSITION FORM

For use of this form, see AR 340-15; the proponent agency is TAGO.

REFERENCE OR OFFICE SYMBOL	SUBJECT
SLCBR-TB	Submission of Manuscript for Publication

TO Chief, STINFO (Tech Reports)   **FROM** TBD   **DATE** 9 June 1988   **CMT 1**

1. The enclosed manuscript is submitted for publication, as follows:

   - This report does _____ does not _X_ supersede an IMR. IMR No. ___ dated _____.

   b. Title: <u>Axisymmetric Calculations for the Large Blast/Thermal Simulator (LB/TS)</u> <u>Shock Tube Configuration</u>

   c. BRL Author(s): <u>Hisley, Dixie M.</u>

      Non-BRL Author(s): <u>Molvik, Gregory A.</u>

   d. Report Classification: <u>Unclassified</u>

      Classified by: _____

   e. The following distribution will be applied to this report:

   A <u>X</u>   D ___   Reason: _____
   B ___   E ___
   C ___   _____

   f. Project No: <u>1L162120AH25</u>

   g. Remarks: _____

   h. Type of Report: TR <u>X</u>   MR ___   CR ___   SP ___   IMR ___

   i. Report was composed on (type of machine used): <u>Zenith/Jove editor</u>,
   using a (type of element/type style) <u>Laser printer font 404</u>.

2. We attest to the accuracy of technical content and security classification of the enclosed manuscript, and are satisfied with its technical organization. We, the undersigned, submit this report for publication.

   Author(s)/COR   *Dixie M Hisley* , *Dixie M Hisley for Gregory A Molvik*

   Reviewer(s)   *Richard E Lottero*   *Michael J Nusca*

               CLARENCE W. KITCHENS, JR.
               Chief

Encl

Branch Chief   ANDREW MARK, Chief, Blast Dynamics Branch, TBD

SLCBR Form 3R, 1 Jun 86

DA FORM AUG 80 **2496**   PREVIOUS EDITIONS WILL BE USED   • USGPO 1986—490-003/432-1

TABLE OF CONTENTS

Page

LIST OF FIGURES

LIST OF FIGURES

1. INTRODUCTION

Computational fluid dynamics (CFD) is a tool which predicts the gas dynamics of blast problems of interest to the Army by solving a set of mathematical equations with a high-speed digital computer. The governing equations for the blast problem presented here are the two-dimensional unsteady Euler equations. The computations were performed on a Cray XMP/48 supercomputer by discretizing the Euler equations with an upwind, Total Variation Diminishing (TVD), finite-volume, implicit scheme. In a paper by Molvik,(1)* the scheme was presented in detail and proved to be well suited for blast wave calculations. The scheme is discussed in the computational algorithm section. The algorithm is used here to provide gas dynamic information for a candidate Large-Scale Blast and Thermal Simulator (LB/TS) concept.

The Army has a growing need for nuclear blast and thermal survivability testing of tactical equipment. In order to meet this need, the Army is conducting research into the design and operation of a Large-Scale Blast and Thermal Simulator (LB/TS), essentially a large multi-driver shock tube with thermal capabilities. The LB/TS design(2) currently consists of a number of driver tubes releasing compressed gas through a series of converging-diverging nozzles into a large expansion tunnel, Figure 1. The compressed gas forms a shock which travels down the expansion tunnel and produces the blast simulation. The thermal simulation is accomplished by igniting a Thermal Radiation Source (TRS) based on aluminum/oxygen combustion just before the arrival of the blast wave at the test section. The expansion tunnel is physically large enough to accommodate the testing of full-sized tactical vehicles such as tanks and helicopters at low blockage of the test section.

The LB/TS can be modeled in a 2-D axisymmetric sense by combining the drivers and nozzles to form one equivalent driver as shown in Figure 3. This simplified model of the LB/TS was actually built for experimental testing at Aberdeen Proving

----

* The numbers inside ( ) denote the reference number.

Ground. The thermal radiation source was not experimentally or computationally modeled. This shock tube is 1/57th of the scale of the proposed LB/TS. The experimental data obtained in this tube was used for LB/TS design studies and BLAST2D code validation. All of the experimental and computational data presented in this paper was from this shock tube configuration. Blast waveforms were produced with peak overpressures ranging from approximately 5 psi to 35 psi. Heating of the driver gas was performed for some of the high pressure cases to reduce the driver pressure required to obtain a given shock overpressure, and to alleviate the temperature (density) discontinuity at the contact surface between the expanded driver gas and shocked expansion section gas.

Currently, one-dimensional calculations have been performed for the 1/57 scale LBS with useful results.(3,4) However, the one-dimensional calculations have had limited success for accurately predicting the flow through the diverging portion of the LBS design because the flow in this region is multi-dimensional. The flow is multi-dimensional due to the rapid and large area change that exists in the diverging nozzle. The remainder of this paper presents the upwind, TVD, finite-volume, implicit scheme in the BRL BLAST2D code and results which capture and reveal the nature of the flow physics in the 1/57 scale LBS.

2. GOVERNING EQUATIONS

The governing equation is the Euler equation written in integral form:

$$\frac{d}{dt} \int_V Q dV + \int_S n \cdot F dS = 0 \tag{1}$$

The integral form of the Euler equation can be rewritten for a two-dimensional generalized cell volume (Figure 3) as :

$$0 = \frac{d}{dt} \int_V Q dV + \int_{j-\frac{1}{2}}^{j+\frac{1}{2}} \left(E_{i+\frac{1}{2}} - E_{i-\frac{1}{2}} \right) d\eta + \int_{i-\frac{1}{2}}^{i+\frac{1}{2}} \left(F_{j+\frac{1}{2}} - F_{j-\frac{1}{2}} \right) d\xi \tag{2}$$

2

where;

$$Q = \begin{pmatrix} \rho \\ \rho u \\ \rho v \\ e \end{pmatrix} \quad E = \begin{pmatrix} \rho U \\ \rho U u + Y_\eta p \\ \rho U v - x_\eta p \\ (e+p)U \end{pmatrix} \quad F = \begin{pmatrix} \rho V \\ \rho V u - y_\xi p \\ \rho V v + x_\xi p \\ (e+p)V \end{pmatrix} \tag{3}$$

This set of four integral equations represents the conservation of mass, momentum in x and y directions, and energy, per unit volume where ρ is the density, p is the pressure, u and v are the velocities in the x (longitudinal) and y (height) directions respectively, and e is the total internal energy per unit volume:

$$e = \frac{p}{(\gamma-1)} + 1/2 \, \rho(u^2 + v^2) \tag{4}$$

The volume fluxes are defined as:

$$U = y_\eta u - x_\eta v \tag{5}$$

$$V = y_\xi u + x_\xi v \tag{6}$$

For the two dimensional cell shown in Figure 3, the integration of flux over the surface in Equation 1 has been replaced in Equation 2 by an integral over each face of the cell. The η-direction is taken as the body normal and the ξ-direction is tangential to the surface of the body. The cell volume and walls are assumed to be fixed in time. The metrics $x_\xi, y_\xi, x_\eta, y_\eta$ are the vector elements of the cell walls and V is the volume of the grid cell.

The physical, independent variables (x,y,t) were transformed into a uniformly spaced computational grid (ξ, η, τ) by a general transformation of the form:

3

$$\tau = t$$

$$\xi = \zeta(t,x,y)$$

$$\eta = \eta(t,x,y) \qquad (7)$$

The transformations were chosen so that the grid spacing in the computational space is uniform and of unit length, $\Delta\xi = 1$, $\Delta\eta = 1$. Thus, the uniform equi-spaced mesh in psi and eta allows the use of unweighted differencing schemes. As a result, the computational code can be applied to a variety of physical geometries and grids.

If an average flux is defined on the cell faces, and $\Delta\xi$ and $\Delta\eta$ are taken as unity, the integral form of the Euler equation, Equation 2 can be rewritten in finite volume form as:

$$V_{i,j} \frac{\overline{Q}^{n+1}_{i,j} - \overline{Q}^{n}_{i,j}}{\Delta\tau} + \frac{\hat{E}^{m}_{i+\frac{1}{2},j} - \hat{E}^{m}_{i-\frac{1}{2},j}}{\Delta\xi} + \frac{\hat{F}^{m}_{i,j+\frac{1}{2}} - \hat{F}^{m}_{i,j-\frac{1}{2}}}{\Delta\eta} = 0 \qquad (8)$$

where the indices i and j correspond to the ξ and η directions respectively in the computational mesh as shown in Figure 3. The vectors E and F are the convective numerical fluxes in computational space (ξ,η,τ) consistent with the physical fluxes E and F in (x,y,t). The vector Q consists of the cell averaged dependent variables. The integration scheme is fully implicit if m=n+1 and is explicit if m=n. The variables have been nondimensionalized as follows;

4

$$\tilde{x} = \frac{x}{L} \qquad \tilde{u} = \frac{u}{c_1} \qquad \tilde{p} = \frac{p}{\rho_4 c_1^2}$$

$$\tilde{y} = \frac{y}{L} \qquad \tilde{v} = \frac{v}{c_1} \qquad \tilde{e} = \frac{e}{\rho_4 c_1^2} \qquad (9)$$

$$\tilde{\rho} = \frac{\rho}{\rho_4} \qquad \tilde{t} = \frac{t c_1}{L}$$

where L=1, c=sound speed, and subscripts 1 and 4 represent
conditions in the driven and driver sections respectively.

3. THE COMPUTATIONAL ALGORITHM

3.1 _Introduction_. Discretization of the governing
equations into an upwind, TVD, finite-volume, implicit scheme
produces an algorithm that is well suited for blast wave
calculations.(1) Upwind flux difference splitting with TVD
achieves second-order accuracy without introducing spurious
oscillations near discontinuities. Strong gradients and
complex flow fields are resolved accurately. Older techniques
used central differencing schemes with arbitrary smoothing
parameters which could not be relied on to capture strong
gradients (i.e., pressure ratio across the shock > 10.0)
accurately.(5) The advantages of the central differencing
techniques were programming simplicity and adequate resolution
for weak gradient problems. However, for the complex flow
fields and strong gradients typical of blast problems upwind
differencing with TVD provides better resolution. The
disadvantages of upwind differencing with TVD are long
computing times caused by an increase in the number of
arithmetic operations per integration step and loss of
programming simplicity. The BLAST2D code results shown in this
paper were generated on a Cray XMP/48 and typically took six
to seven hours of cpu time.

Conservative schemes capture shocks and other
discontinuities automatically. The finite volume philosophy
ensures conservation at interior and boundary points. The
scheme is made implicit by linearizing only the first-order

5

contribution and by employing a Newton iteration of the type
described by Rai(5) to eliminate any approximations made. The
implicit version of the scheme requires more computations per
integration step than the explicit version, but permits larger
time steps which overall reduces computational expense.

The next section presents the first-order accurate upwind
scheme(1) which is the basic building block of the
computational algorithm. Subsequently, the first-order scheme
is expanded to second order accuracy with the addition of
second-order terms and TVD concepts. Development of the
implicit version of the algorithm and the Newton iterative
procedure used is presented. Finally, boundary conditions are
discussed briefly.

3.2 **First-Order Scheme**. The first-order scheme is
based upon Roe's approximate Riemann solver (6,7) coupled with
upwind flux difference splitting. First, approximate Riemann
solvers are discussed. Then, the information supplied by the
Riemann solver is used with upwind flux difference splitting
concepts to provide the first-order convective fluxes E and F
in the finite volume form of the Euler equation, Equation 8.

Riemann problems are incorporated into the numerical
solution by considering the dependent variables at cell
centers for each cell in turn, as pairs of states defining a
sequence of Riemann problems, Figure 4. The Riemann problem
for the ξ direction in Figure 4 is : given two states
$(\rho 1, u1, p1)$ and $(\rho 4, u4, p4)$ determine the combination of shocks,
contact discontinuities, and expansions which result in these
end states, that is, determine $(\rho 2, u2, p2)$ and $(\rho 3, u3, p3)$. To
obtain a solution, exact Riemann solvers require an iterative
procedure which is computationally expensive when performed
for a large number of cells and time steps. The expense of
producing an exact solution to the Riemann problem is
justified only if the information made available could be put
to some sophisticated use. The approximate Riemann solvers are
considerably less expensive because the Riemann problem is
solved with a direct non-iterative method which is about as
time consuming as one cycle of the iterative procedures.
Comparisons of the solutions from the exact vs. approximate
Riemann solvers reveal slight differences. Other approximate
Riemann solvers could have been used, but Roe's method is
the approach recommended by Chakravarthy when computational

6

efficiency is important.(6)

References 6 and 7 outline in detail Roe's method for determining the intermediate states of the Riemann problem. In general, the solution consists of four constant property states separated by three waves, Figure 4. Once the dependent variables are obtained at the intermediate states, the flux at the cell interface is calculated by determining the flux change across the waves. The flux change associated with the waves traveling in the positive ξ direction is given the symbol ΔE^+ and that in the negative direction is represented by ΔE^-. The waves carry information from the "upwind" direction to the cell center, thus the notion of upwind differencing. The flux remaining at the interface for all time associated with this Riemann problem must then be represented by either of the following equations:

$$\hat{E}_{i+\frac{1}{2}} = E_i + \Delta E^-_{i+\frac{1}{2}} \tag{10}$$

$$\hat{E}_{i+\frac{1}{2}} = E_{i+1} - \Delta E^+_{i+\frac{1}{2}} \tag{11}$$

or, by averaging the two equations above,

$$\hat{E}_{i+\frac{1}{2}} = 1/2 \left(E_i + E_{i+1} + \Delta E^-_{i+\frac{1}{2}} - \Delta E^+_{i+\frac{1}{2}} \right) \tag{12}$$

Let Λ, R, and R^- denote the eigenvalue matrix, and the right and left eigenvector matrices respectively, evaluated at the cell interface.(7) The flux difference across the positive and negative velocity waves can be calculated. They are:

$$\Delta E^+_{i+\frac{1}{2}} = \left(R_{i+\frac{1}{2}} \left(\Lambda + |\Lambda| \right)_{i+\frac{1}{2}} R^{-1}_{i+\frac{1}{2}} \right) \left(\overline{Q}_{i+1} - \overline{Q}_i \right) = A^+ \left(\overline{Q}_{i+1} - \overline{Q}_i \right) \tag{13}$$

$$\Delta E^-_{i+\frac{1}{2}} = \left(R_{i+\frac{1}{2}} \left(\Lambda + |\Lambda| \right)_{i+\frac{1}{2}} R^{-1}_{i+\frac{1}{2}} \right) \left(\overline{Q}_{i+1} - \overline{Q}_i \right) = A^- \left(\overline{Q}_{i+1} - \overline{Q}_i \right) \tag{14}$$

However, the dependent variables are not defined at the cell

interfaces where these matrices must be evaluated. Roe(7) has developed a special averaging process to calculate the dependent variables on the cell interface and satisfy the following relation.

$$\hat{E}_{i+1} - \hat{E}_i = [A]^{Roe}_{i+\frac{1}{2}} \left(\overline{Q}_{i+1} - \overline{Q}_i \right)$$

$$= [A^+ + A^-]^{Roe}_{i+\frac{1}{2}} \left(\overline{Q}_{i+1} - \overline{Q}_i \right)$$

(15)

The superscript Roe denotes a Roe averaged quantity. By satisfying the relations above, the shock capturing capabilities of the algorithm are retained and correct wave speeds are assured. Roe's averaging of the dependent variables proceeds as follows:

$$u_{i+\frac{1}{2}} = \frac{u_i \sqrt{\rho_i} + u_{i+1} \sqrt{\rho_{i+1}}}{\sqrt{\rho_i} + \sqrt{\rho_{i+1}}} \qquad v_{i+\frac{1}{2}} = \frac{v_i \sqrt{\rho_i} + v_{i+1} \sqrt{\rho_{i+1}}}{\sqrt{\rho_i} + \sqrt{\rho_{i+1}}}$$

$$h_{i+\frac{1}{2}} = \frac{h_i \sqrt{\rho_i} + h_{i+1} \sqrt{\rho_{i+1}}}{\sqrt{\rho_i} \quad \sqrt{\rho_{i+1}}}$$

$$c_{i+\frac{1}{2}} = \left\{ \left(h_{i+\frac{1}{2}} - 1/2 \left(u^2_{i+\frac{1}{2}} + v^2_{i+\frac{1}{2}} \right) \right) (\gamma-1) \right\}^{\frac{1}{2}}$$

(16)

where the total enthalpy per unit mass is

$$h = (e + p)/\rho$$

(17)

The first-order flux on the j+1/2 interface can be obtained in a similar manner by replacing x_ξ with $- x_\eta$ and y_ξ with $-y_\eta$.

3.3 Second-Order Scheme. A second-order convective flux can be produced by adding a correction term to the first-order flux. However, in order to avoid spurious oscillations, the correction term must fulfill the criteria for the algorithm to be TVD. TVD schemes achieve second-order accuracy without introducing spurious oscillations near discontinuities by employing a feedback mechanism -"smart numerical dissipation"- wherein fluxes are compared at neighboring control volumes. In regions of little change no numerical dissipation is added to the second order correction

8

terms, while in regions of large change, numerical dissipation is added to ensure stability.

During this process no new extrema are created by the numerical dissipation. TVD data preserve monotonicity; a) no new extrema must be created and b) the absolute value of any extrema must not increase. TVD schemes yield oscillation-free solutions by modifying flux differences to meet the above criteria. Reference 7 outlines a class of explicit flux limiting schemes that fulfill this criteria. The second-order flux for the fully upwind scheme can be written as(1):

$$\hat{E}^{2nd}_{i+\frac{1}{2}} = \hat{E}^{1st}_{i+\frac{1}{2}} + 1/2 \left[\Delta \widetilde{\widetilde{E}}^{+}_{i-\frac{1}{2}} - \Delta \widetilde{E}^{-}_{i+3/2} \right] \qquad (18)$$

If the following definitions are made,

$$\Delta \sigma^{+}_{i+\frac{1}{2}} = \left((\Lambda + |\Lambda|)_{i+\frac{1}{2}} \; R^{-1}_{i+\frac{1}{2}} \right) \left(\overline{Q}_{i+1} - \overline{Q}_i \right) \qquad (19)$$

$$\Delta \sigma^{-}_{i+\frac{1}{2}} = \left((\Lambda + |\Lambda|)_{i+\frac{1}{2}} \; R^{-1}_{i+\frac{1}{2}} \right) \left(\overline{Q}_{i+1} - \overline{Q}_i \right) \qquad (20)$$

then the limited values of the flux can be written as

$$\Delta \widetilde{E}^{-}_{i+\frac{1}{2}} = R_{i+\frac{1}{2}} \; \Delta \widetilde{\sigma}^{-}_{i+\frac{1}{2}} \; , \; \Delta \widetilde{\widetilde{E}}^{+}_{i+\frac{1}{2}} = R_{i+\frac{1}{2}} \; \Delta \widetilde{\widetilde{\sigma}}^{+}_{i+\frac{1}{2}} \qquad (21)$$

Note that the characteristic fluxes are limited, not the fluxes given in Equation 3. The symbols $\sim$ and $\approx$ shown over the $\Delta \sigma$ denote flux-limited values of $\Delta \sigma$ and are computed as follows:

$$\Delta \widetilde{\sigma}^{-}_{i+\frac{1}{2}} = minmod \left[\Delta \sigma^{-}_{i+\frac{1}{2}} \; , \; \beta \Delta \sigma^{-}_{i-\frac{1}{2}} \right] \qquad (22)$$

$$\Delta \widetilde{\widetilde{\sigma}}^{+}_{i+\frac{1}{2}} = minmod \left[\Delta \sigma^{+}_{i+\frac{1}{2}} \; , \; \beta \Delta \sigma^{+}_{i+3/2} \right] \qquad (23)$$

Where the "minmod" is defined as

$$minmod \; [x,y] = sign \; (x) * max \; [0, \; min\{|x|, \; y sign \; (x)\}] \qquad (24)$$

and beta is a compression parameter that is restricted to fall in the range

9

$$1 < \beta \leqslant 2 \qquad (25)$$

Equation 8 can be rewritten with the first-order convective fluxes, E and F, replaced with the second-order fluxes:

$$V_{i,j} \frac{\overline{Q}_{i,j}^{n+1} - \overline{Q}_{i,j}^n}{\Delta \tau} + \left[\frac{\hat{E}_{i+\frac{1}{2},j}^{2nd} - \hat{E}_{i-\frac{1}{2},j}^{2nd}}{\Delta \xi} + \frac{\hat{F}_{i,j+\frac{1}{2}}^{2nd} - \hat{F}_{i,j-\frac{1}{2}}^{2nd}}{\Delta \eta} \right]^n = 0 \qquad (26)$$

The above discussion describes the explicit second-order accurate in space scheme. Second-order accuracy in time is achieved by simply replacing the first-order, backward derivative of the time-dependent variables with a second-order backward difference.

3.4 _Implicit Scheme_. For a fully implicit scheme, the fluxes must be evaluated at the n+1 time level. In order to calculate a flux at the n+1 time level the flux must be linearized with respect to time, t. The first-order numerical flux on the i+1/2 cell interface evaluated at the n+1 time level is represented as:

$$\hat{E}_{i+\frac{1}{2}}^{n+1} = \left[\frac{1}{2} \quad E_{i+1}^{n+1} + E_i^{n+1} + (A^- - A^+)_{i+\frac{1}{2}}^{n+1} (\overline{Q}_{i+1}^{n+1} - \overline{Q}_i^{n+1}) \right] \qquad (27)$$

An approximate linearization of this interface flux may be achieved by freezing the coefficient matrix $(A^- - A^+)$ at time level n and linearizing the remaining terms. Numerical experiments have shown that such an approximation is acceptable. The linearized numerical flux is then written as:

$$\hat{E}_{i+\frac{1}{2}}^{n+1} = \frac{1}{2} \left[A_{i+1}^n + (A^- - A^+)_{i+\frac{1}{2}}^n \right] \Delta \overline{Q}_{i+1} + \frac{1}{2} \left[A_i^n - (A^- - A^+)_{i+\frac{1}{2}}^n \right] \Delta \overline{Q}_i + \hat{E}_{i+\frac{1}{2}}^n \quad (28)$$

$$= (A^R)_{i+\frac{1}{2}}^n \Delta \overline{Q}_{i+1} + (A^L)_{i+\frac{1}{2}}^n \Delta \overline{Q}_i + \hat{E}_{i+\frac{1}{2}}^n$$

where,
$$\Delta \overline{Q}_i = \overline{Q}_i^{n+1} - \overline{Q}_i^n$$

Using a similar type of linearization for the body normal flux, F, as for the streamwise flux, E, the first-order, implicit

10

numerical algorithm is written as:

$$\left\{ \Delta\overline{Q}_{i,j} + \frac{\Delta t}{V_{i,j}} \left[(A^R)^n_{i+\frac{1}{2}}\Delta\overline{Q}_{i+1,j} + \{(A^L)^n_{i+\frac{1}{2}} - (A^R)^n_{i-\frac{1}{2}}\Delta\overline{Q}_{i,j} - (A^L)^n_{i-\frac{1}{2}}\Delta\overline{Q}_{i-1,j} \right] \right.$$

$$\left. + \frac{\Delta t}{V_{i,j}} \left[(B^R)^n_{j+\frac{1}{2}}\Delta\overline{Q}_{i,j+1} + \{(B^L)^n_{j+\frac{1}{2}} - (B^R)^n_{j-\frac{1}{2}}\Delta\overline{Q}_{i,j} - (B^L)^n_{j-\frac{1}{2}}\Delta\overline{Q}_{i,j-1} \right] \right\} \quad (29)$$

$$= - \frac{\Delta t}{V_{i,j}} \left[(\hat{E}^n_{i+\frac{1}{2}j} - \hat{E}^n_{i-\frac{1}{2},j}) + (\hat{F}^n_{i,j+\frac{1}{2}} - \hat{F}^n_{i,j-\frac{1}{2}}) \right]$$

To avoid the expense of inverting a large sparse matrix, an approximate factorization is done to break the banded matrix into two tridiagonal matrices. This is written in two steps with the asterisked * variables denoting an intermediate step as:

$$\Delta\overline{Q}^*_{i,j} + \frac{\Delta t}{V_{i,j}} \left[(A^R)^n_{i+\frac{1}{2}}\Delta\overline{Q}^*_{i+1,j} + \{(A^L)^n_{i+\frac{1}{2}} \right.$$

$$\left. - (A^R)^n_{i-\frac{1}{2}}\}\Delta\overline{Q}^*_{i,j} - (A^L)^n_{i-\frac{1}{2}}\Delta\overline{Q}^*_{i-1,j} \right] = RHS(32) \quad (30)$$

$$\Delta\overline{Q}_{i,j} + \frac{\Delta t}{V_{i,j}} \left[(B^R)^n_{j+\frac{1}{2}}\Delta\overline{Q}_{i,j+1} + \{(B^L)^n_{j+\frac{1}{2}} - (B^R)^n_{j-\frac{1}{2}}\}\Delta\overline{Q}_{i,j} \right.$$

$$\left. + (B^L)^n_{j-\frac{1}{2}}\Delta\overline{Q}_{i,j-1} \right] = \Delta\overline{Q}^*_{i,j} \quad (31)$$

3.5 **Iterative Scheme**. In order to eliminate the linearization and approximate factorization errors that might occur, a Newton iteration technique is employed. The iteration takes the form:

$$\left\{ \Delta\overline{Q}^*_{i,j} + \frac{\Delta t}{V_{i,j}} \left[(A^R)^p_{i+\frac{1}{2}}\Delta\overline{Q}^*_{i+1,j} + \{(A^L)^p_{i+\frac{1}{2}} - (A^R)^p_{i-\frac{1}{2}}\}\Delta\overline{Q}^*_{i,j} - (A^L)^p_{i-\frac{1}{2}}\Delta\overline{Q}^*_{i-1,j} \right] \right\}$$

$$= - (\overline{Q}^p_{i,j} - \overline{Q}^n_{i,j}) - \frac{\Delta t}{V_{i,j}} \left[(\hat{E}^{2nd}_{i+\frac{1}{2},j} - \hat{E}^{2nd}_{i-\frac{1}{2},j}) + (\hat{F}^{2nd}_{i,j+\frac{1}{2}} - \hat{F}^{2nd}_{i,j-\frac{1}{2}}) \right]^p \quad (32)$$

11

$$\left\{ \Delta \overline{Q}_{i,j} + \frac{\Delta t}{V_{i,j}} \left[(B^R)^p_{j+\frac{1}{2}} \Delta \overline{Q}_{i,j+1} + \{(B^L)^p_{j+\frac{1}{2}} - (B^R)^p_{j-\frac{1}{2}}\} \Delta \overline{Q}_{i,j} \right. \right.$$

$$\left. \left. - (B^L)^p_{j-\frac{1}{2}} \Delta \overline{Q}_{i,j-1} \right] \right\} = \Delta \overline{Q}^{\star}_{i,j} \qquad (33)$$

where $\Delta \overline{Q}$ is now defined as the iterative change in the cell averaged dependent variables, $(\overline{Q}^{p+1}_{i,j} - \overline{Q}^{p}_{i,j})$ rather than the time change and p denotes the iteration number. Ideally, all linearization errors are completely eliminated when the residual of equation 31 is driven to zero. However, in practice, convergence is defined short of this with minimal loss in accuracy, in order to reduce the number of iterations and hence the expense of the calculation.

3.6 <u>Axisymmetric Source Term</u>. The governing equations and numerical algorithm described so far are appropriate for 2-D planar problems. It is a simple matter to include axisymmetric effects by adding the source terms denoted by H and I to equation 32 where:

$$H = \frac{1}{r} \begin{bmatrix} \rho v \\ \rho u v \\ \rho v^2 \\ (e+p)v \end{bmatrix} \qquad (34)$$

$$I = \frac{\partial H}{\partial Q} \qquad (35)$$

Thus, equations 32 and 33 become:

$$\left\{ \Delta \overline{Q}^{\star}_{i,j} + \frac{\Delta t}{V_{i,j}} \left[(A^R)^p_{i+\frac{1}{2}} \Delta \overline{Q}^{\star}_{i+1,j} + \{(A^L)^p_{i+\frac{1}{2}} - (A^R)^p_{i-\frac{1}{2}} + I\} \Delta \overline{Q}^{\star}_{i,j} - (A^L)^p_{i-\frac{1}{2}} \Delta \overline{Q}^{\star}_{i-1,j} \right] \right\}$$

$$= - (\overline{Q}^p_{i,j} - \overline{Q}^n_{i,j}) - \frac{\Delta t}{V_{i,j}} \left[(\hat{E}^{2nd}_{i+\frac{1}{2},j} - \hat{E}^{2nd}_{i-\frac{1}{2},j}) + (\hat{F}^{2nd}_{i,j+\frac{1}{2}} - \hat{F}^{2nd}_{i,j-\frac{1}{2}}) + H \right]^p \qquad (36)$$

12

$$\left\{ \Delta \overline{Q}_{i,j} + \frac{\Delta t}{V_{i,j}} \left[(B^R)_{j+\frac{1}{2}}^p \Delta \overline{Q}_{i,j+1} + \{ (B^L)_{j+\frac{1}{2}}^p - (B^R)_{j-\frac{1}{2}}^p + I \} \Delta \overline{Q}_{i,j} \right. \right.$$

$$\left. \left. - (B^L)_{j-\frac{1}{2}}^p \Delta \overline{Q}_{i,j-1} \right] \right\} = \Delta \overline{Q}_{i,j}^* \qquad (37)$$

3.7 <u>Boundary Conditions</u>. The inviscid boundary conditions are obtained by specifying an appropriate flux on the walls of the shock tube and at the symmetry boundary. Only half of the symmetrical shock tube is actually modeled to save computational expense. Then, the results are graphically reflected. At the walls and symmetry boundary, the normal component of velocity is zero, the tangential component of velocity is nonzero. The flux on these surfaces can then be represented as:

$$F = \begin{bmatrix} 0 \\ -y_\xi p \\ x_\xi p \\ 0 \end{bmatrix} \qquad (38)$$

Only a value of pressure need be evaluated at the surface. As a first approximation, one might consider using the pressure of the cell directly above the surface. This translates into a zero-order approximation. However a first-order approximation of the surface flux can be made if a Riemann problem is set up on the surface. This is consistent with the interior scheme and would seem like the reasonable approach. The first-order Riemann solver is used between the first cell off the surface and a reflected cell. If the subscripts 1 and -1 denote the first cell off the surface and the reflected cell respectively, the surface flux can then be written as:

$$\hat{F}_s = 1/2 \left[F_1 + F_{-1} + \left(A^- - A^+ \right)_s \left(\overline{Q}_1 - \overline{Q}_{-1} \right) \right] \qquad (39)$$

13

The dependent variables of the reflected cell are calculated using the following relations.

$$\rho_{-1} = \rho_1 \qquad\qquad p_{-1} = p_1$$

$$u_{-1} = \left[\left(x_\xi^2 - y_\xi^2\right)u_1 + 2x_\xi y_\xi v_1\right]\Big/\left[x_\xi^2 + y_\xi^2\right] \qquad (40)$$

$$v_{-1} = \left[\left(y_\xi^2 - x_\xi^2\right)v_1 + 2x_\xi y_\xi u_1\right]\Big/\left[x_\xi^2 + y_\xi^2\right]$$

The metrics in the above equations are those of the cell interface on the surface. A second order flux can be obtained by reflecting even another set of dependent variables with a subscript of -2.

4. GEOMETRY, GRID, AND INITIAL CONDITIONS FOR LBS COMPUTATION

The geometry of the single-driver, 1/57 scale model LBS design concept is shown in Figure 2. The corners and sharp edges were smoothed out in the computational shock tube to simplify grid generation and to facilitate the use of an elliptic grid generator for the driver and converging-diverging nozzle portion of the tube. The elliptic grid generator produced grid cells that varied smoothly in regions of rapid change such as the converging-diverging nozzle. The grid generated for this configuration was 488 cells axially and 30 cells radially. The computational and experimental diaphragm and test station locations were the same as shown in Figure 2.

Five computations were performed for the LBS configuration with initial conditions that duplicated experimental runs. The initial conditions are summarized in the following table:

TABLE 1. 1/57 Scale Model LBS Initial Conditions

Shot #	P4/P1	Heated Driver	T4/T1	Overpressure kPa (psi)
2	16.0	no	1.0	34 (5)

12	136.0	no	1.0	175 (25)
85-11	68.6	yes	1.58	175 (25)
85-21	224.4	no	1.0	241 (35)
85-23	132.1	yes	1.84	241 (35)

5. RESULTS AND DISCUSSION

Computational results are presented in this section for the five initial conditions listed in Table 1. The five conditions represent possible lower and upper limits of blast simulation under consideration for the LB/TS. The 175 kPa and 241 kPa pressure levels are more difficult to computationally simulate than the 34 kPa level because of the increased complexity of the resulting flow gradients. Comparisons with experimental data are made where possible.

Data is presented in the form of overpressure and dynamic pressure versus time plots at station 7. Station 7 is located seven diameters downstream from the end of the diverging nozzle and is the primary test location. Also, density and pressure contour plots are presented. The density and pressure contour plots reveal the nature of the flow physics in the shock tube. In this study, efforts are concentrated on understanding two flow phenomena; one is the nozzle flow that results in the large blast thermal simulator, the second is the flow differences that result when the driver gas is heated versus when the driver gas is not heated.

The pressure versus time plots for the 34 kPa (5 psi) run are presented in Figure 5. An experimental dynamic pressure record was not available for this case, therefore, the stagnation pressure record was substituted. The experimental probe was positioned at one half the radius of the tube. The computational data sampled at one half the radius reveals excellent agreement while the computational data sampled at the centerline is in poor agreement. This implies that the stagnation pressure in the radial direction is nonuniform. The stagnation pressure versus time plot shows the importance of computationally sampling at the same spanwise position in the tube as the experiment.

16

The static overpressure plot shows a discrepancy between the experimental and computational data on the end of the positive phase duration (time when static overpressure goes negative). The experimental and computational data indicates the end of the positive phase duration at 26 and 18 ms respectively. The volume of the computational driver after grid generation was slightly smaller than the volume of the experimental driver, which could cause this discrepancy. Otherwise, the computational and experimental data on the pressure versus time plots are in excellent agreement. Note the computational data is taken at 1/4 diameter and at the centerline. The experimental data was taken by probes flush with the tube wall. This excellent comparison indicates that the static overpressure is radially uniform in the tube. In this paper, the computational and experimental comparison of static overpressure produced very good agreement at all shock overpressures.

The contour data for the 34 kPa (5 psi) run, Figures 6 through 8, reveal the formation of a complex shock system in the diverging nozzle. The contour data shows the primary shock, contact surface, and backward-facing shock developing in the diverging nozzle. The backward-facing shock is not a normal shock, but consists of two oblique shocks which terminate in a normal shock at the center of the tube. The intersection of the oblique and normal shock produces a reflected or an oblique transmitted shock which can also be seen in the contour plots, Figure 7. The complex structure of the backward-facing shock has been verified experimentally, as shown in a shadowgraph photograph by Amann(8), Figure 9.

The primary shock moves quickly through the diverging nozzle and proceeds downstream as a normal shock. The contact surface which separates the driver gas from driven gas can be distinguished as the clustered gradient present in the density plot and not present in the pressure plot. The contact surface moves downstream, maintaining a curved surface. Behind it, the driver gas resembles core flow. In Figure 8, the contact surface takes on a jetting appearance at the centerline boundary that may be an artifice of the code. Behind the contact surface, a complex system of oblique

shocks, rotational motion and slip surfaces develops in the core flow.

The oblique shocks are a result of the backward facing shock, which remains in the diverging nozzle, reflecting at the solid walls and symmetry boundary as oblique shocks. These reflections set up a shock diamond pattern that stretches downstream. This shock diamond pattern was discussed by Gottlieb(9), "If the conical expansion is too rapid, however, or boundary-layer effects are significant this upstream-facing shock wave would be a series of cells consisting of oblique shock waves. The spatial extent or length of such pseudo-shock patterns is very large compared to the thickness of a typical normal shock wave, and they can cover a duct length of many tube diameters". The computations presented here were inviscid, which implies the rapid expansion alone can produce the shock diamond pattern shown in the contour plots.

Even though this is an inviscid code, rotational motion can occur, as visible in Figure 8. Gradients in total enthalpy are caused by the unsteady nature of the shock. These gradients in entropy occur when some streamlines experience a higher entropy increase by going through the normal part of the recompression shock while other streamlines experience a lower entropy increase by going through the oblique part of the recompression shock. From Crocco's theorem we know that whenever gradients in total entalpy or gradients in entropy exist in the flow field, rotational motion occurs.

Figures 10 through 13 present pressure versus time results for the 175 kPa (25 psi) and 241 kPa (35 psi) unheated and heated runs. As stated before, the computational and experimental comparison of static pressure produced good agreement at all shock overpressures. However, it is very important for blast simulation to model not only static pressure but dynamic pressures as well.

Experimental dynamic pressure is not measured directly in the shock tube but is calculated from static and stagnation pressure records. The static pressure data was measured at the wall and the stagnation pressure data was measured at 1/4 diameter. To be rigorous, the static and stagnation probes

17

should be at the same location in order to calculate true local Mach number and thus true dynamic pressure. However, if the static pressure is radially uniform, then there is no need to have the probes at the same exact radial location. The code indicates static pressure is radially uniform, although this has not been confirmed experimentally by placing probes at different radial locations.

For the 175 kPa heated driver case, the experimental and computational comparison of dynamic pressure are in excellent agreement until the contact surface goes by at .008 seconds. After the contact surface, the computation at 1/4 diameter and the experimental record, based on a stagnation probe at 1/4 diameter are very similar except for one anomaly. The motivation for heating the driver gas can be seen in the experimental records for the 175 kPa unheated driver case.

For the 175 kPa unheated driver case, a much noisier experimental dynamic pressure record is indicated after the arrival of the contact surface. In the previous case, heating smoothed this region and produced a simulation closer to that of a decaying free field wave. Computationally, the comparison is good until the arrival of the contact surface, After the contact surface, the experiment shows a higher Mach number flow at the centerline.

The purpose of heating is to reduce the jump in dynamic pressure (Figures 10 and 12) which occurs across the contact surface for unheated cases. The jump in dynamic pressure increases with the shock overpressure.(2) When the diaphragm is opened, the driver gas is cooled by the passage of the rarefaction wave into the driver section. The driven gas is heated by the passage of the primary shock. At the contact surface, where the driver gas meets the driven gas, the difference in temperature of the driver and driven gas results in a difference in density which in turn is demonstrated as a jump in the dynamic pressure plots. By heating the driver gas to the proper level, the temperature on each side of the contact surface can be matched.

Furthermore, heating of the driver gas reduces the driver pressure required to obtain a given shock overpressure as shown by the initial conditions in Table 1. Heating also significantly reduces the spike activity in the stagnation and

18

dynamic pressure versus time records (Figures 11 and 13) and produces overpressure versus time records that more closely resemble a smoothly decaying blast overpressure wave shape.

Figures 14 through 19 present contour plots for the 175 kPa (25 psi) and 241 kPa (35 psi) unheated and heated runs. Another effect of heating, as shown in the last contour plots (Figures 16 and 19) available for the time simulated, is the backward-facing shock is eventually swallowed in the nozzle for the heated case, but remains outside the nozzle for the unheated case.

VI. Conclusions

One-dimensional calculations(3,4) have had limited success for accurately predicting the flow through the rapid expansion of the LB/TS design because the flow in this region is multi-dimensional. Two-dimensional calculations with the upwind, TVD, finite-volume, implicit scheme in the BRL BLAST2D code were presented here which captured and revealed the nature of the flow physics in the 1/57 scale LBS. A complex system of shocks, vortices, and slip surfaces were revealed in contour plots.

Nozzle flow produces a complex recompression shock system which influences the flow behind the contact surface. The static pressure is uniform radially, however, the stagnation pressure and thus both the Mach number and dynamic pressure vary greatly. Because of this radial variation in flow it is very important to compare dynamic pressure computational and experimental records at the same radial location. Heating reduces the required driver pressure for a given shock overpressure and smooths the flow behind the contact surface, producing a dynamic pressure record closer to that of a free field wave.

The BLAST2D code provides excellent modeling capability at low shock overpressures and good modeling capabilities at higher shock overpressures. The code simulates heated driver cases better than unheated driver cases for high shock overpressures. Future efforts will be concentrated on

including viscous effects in the simulations and better modeling and understanding of dynamic pressure at high shock overpressures.

REFERENCES

1. G. A. Molvik, "Computation of Viscous Blast Wave Solutions with an Upwind Finite Volume Method", AIAA Paper 87-1290, Honolulu, HA, June 1987.

2. R. Pearson, K. Opalka, and D. Hisley, "Design Studies of Drivers for the US Large Blast/Thermal Simulator", Proceedings of the Ninth International Symposium on Military Applications of Blast Simulation (MABS9), Oxford, England, 23-27 September, Atomic Weapons Research Establishment, Foulness, Southend-on-Sea, Essex, England SS3 9XE.

3. E. Gion, D. Hisley and B. Bertrand, "Experimental and Theoretical Performance of Large Blast Simulator Models", Proceedings of the Ninth International Symposium on Military Applications of Blast Simulation (MABS9), Oxford, England, 23-27 September, Atomic Weapons Research Establishment, Foulness, Southend-on-Sea, Essex, England SS3 9XE.

4. K.O. Opalka and A. Mark, "The BRL-Q1D Code: A Tool for the Numerical Simulation of Flows in Shock Tubes with Variable Cross-Sectional Areas", BRL-TR-2763, US Army Ballistic Research Laboratory, Aberdeen Proving Ground, Maryland, 21005, October 1986.

5. M. M. Rai, "An Implicit Form for the Osher Upwind Scheme", AIAA Paper 84-0088, Reno, NV, Jan. 1984.

6. S. R. Chakravarthy, "A New Class of High Accuracy TVD Schemes for Hyperbolic Conservation Laws", AIAA Paper, 85-0363, Reno, NV, Jan. 1985.

7. P. L. Roe, "Approximate Riemann Solvers, Parameter Vectors, and Difference Schemes", Journal of Computational Physics, Vol. 43, 1981, pp. 357-372.

8. Amann, in An Albumn of FLuid Motion, Van Dyke, ed., The Parabolic Press, Post Office Box 3032, Stanford, CA 94305, p. 171.

9. J. J. Gottlieb, "Random-Choice-Method Computations of LB/TS Design", Aerospace Engineering and Research Consultants Limited, 4925 Dufferin Street, Downsview, Ontario M3H 5T6, 29 March 1986.

CURRENT US LARGE BLAST/THERMAL SIMULATOR CONCEPT

CONCRETE
STEEL
SOIL

1 - HEATED, STEEL DRIVER TUBES
2 - ADJUSTABLE END PLATES
3 - BAFFLES
4 - CONCRETE REACTION PIER
5 - CONVERGENT NOZZLE
6 - DIAPHRAGMS
7 - VALVES FOR VENTING
8 - DIVERGENT NOZZLE
9 - STRESS CONCRETE EXPANSION TUNNEL

10 - ACCESS TUNNEL
11 - STEEL TEST SECTION
12 - THERMAL RADIATION SOURCES
13 - TRS EJECTORS
14 - AIR CURTAIN PLENUM
15 - CAMERA AND LIGHT PORTS
16 - TARGET
17 - SOIL TANK
18 - ACTIVE RAREFACTION WAVE
     ELIMINATOR

Figure 1: Schematic of the Proposed US Large Blast/Thermal Simulator Facility [2]
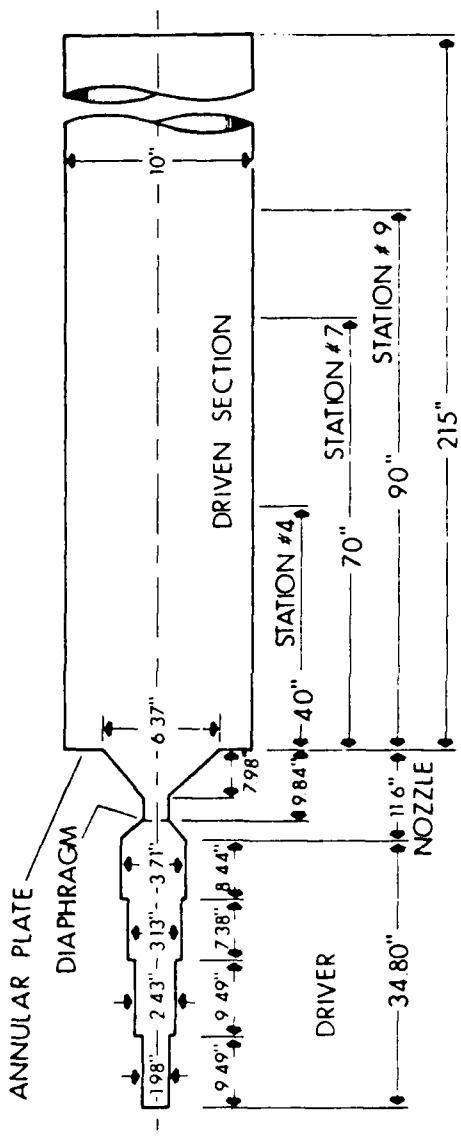
Figure 2: Single-driver 1/57 Scale Model of LBS Design Concept
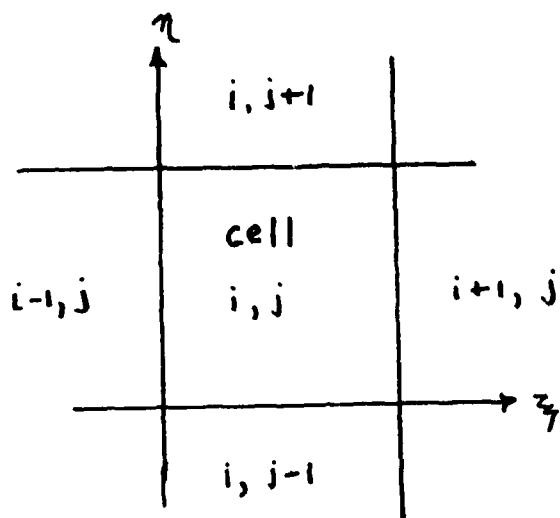
Figure 3: Finite Volume Cell in Computational Space
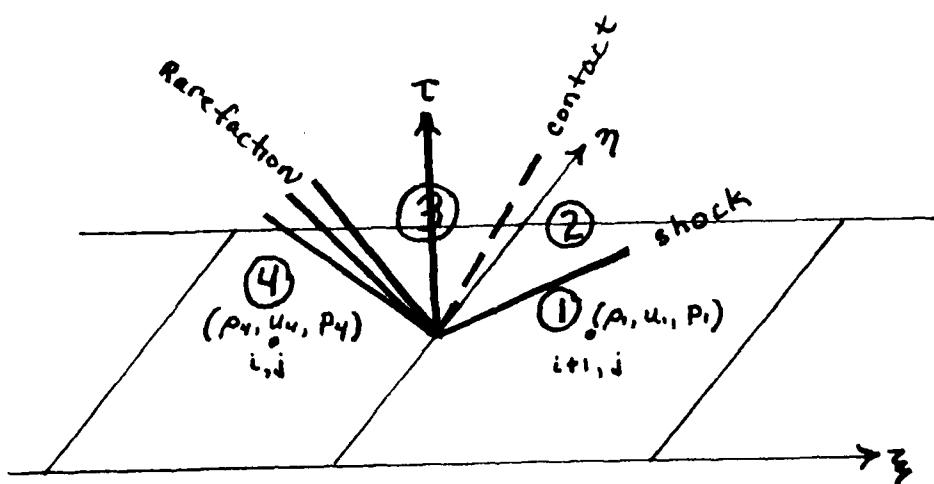
Figure 4: Riemann Problem
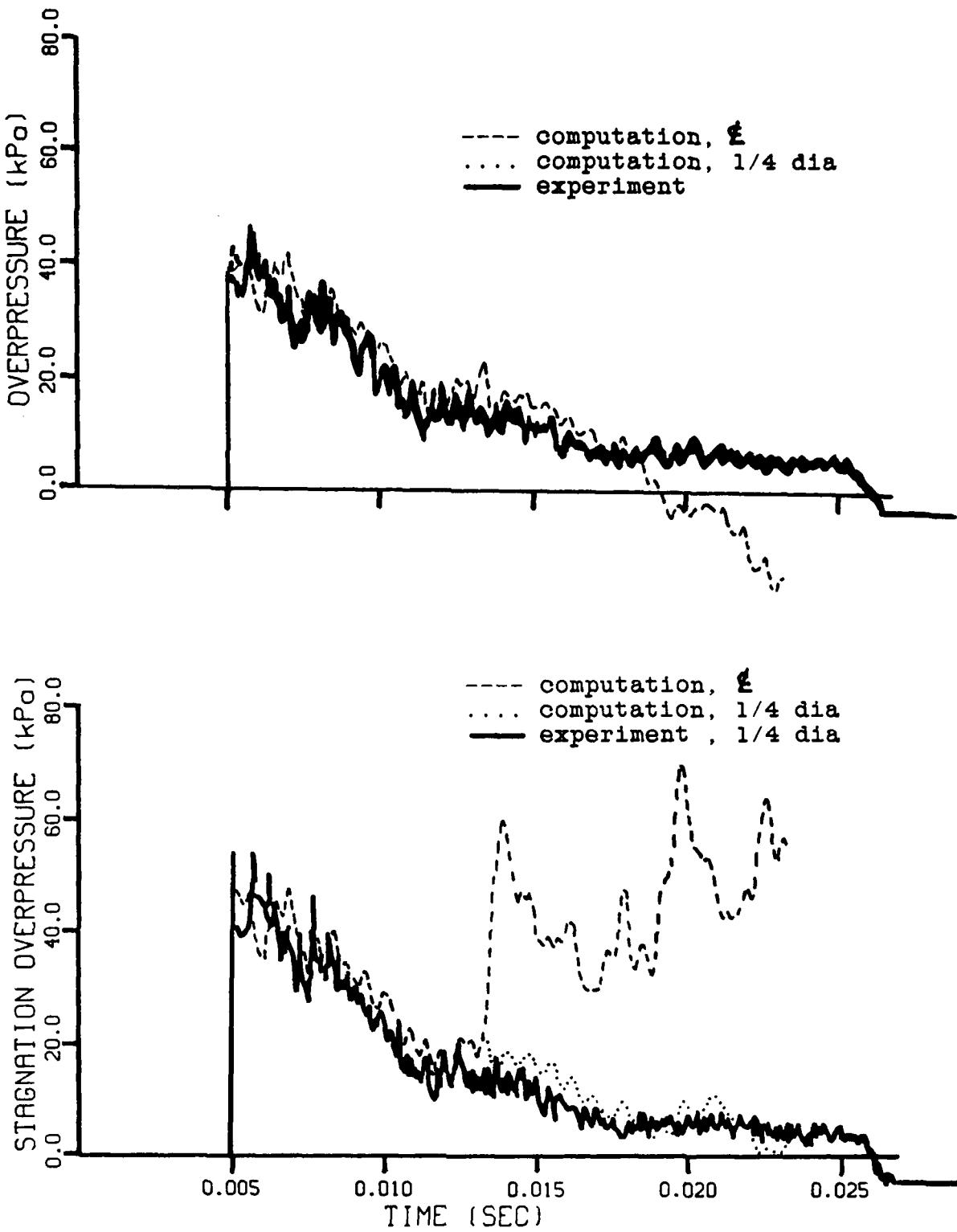
Figure 5: Pressure versus Time Plots, 35 kPa (5 psi)
Peak Overpressure, Shot #2

density   .5 ms

pressure   .5 ms

Contact
surface

density   1.0 ms

Backward-facing   Primary
shock   shock
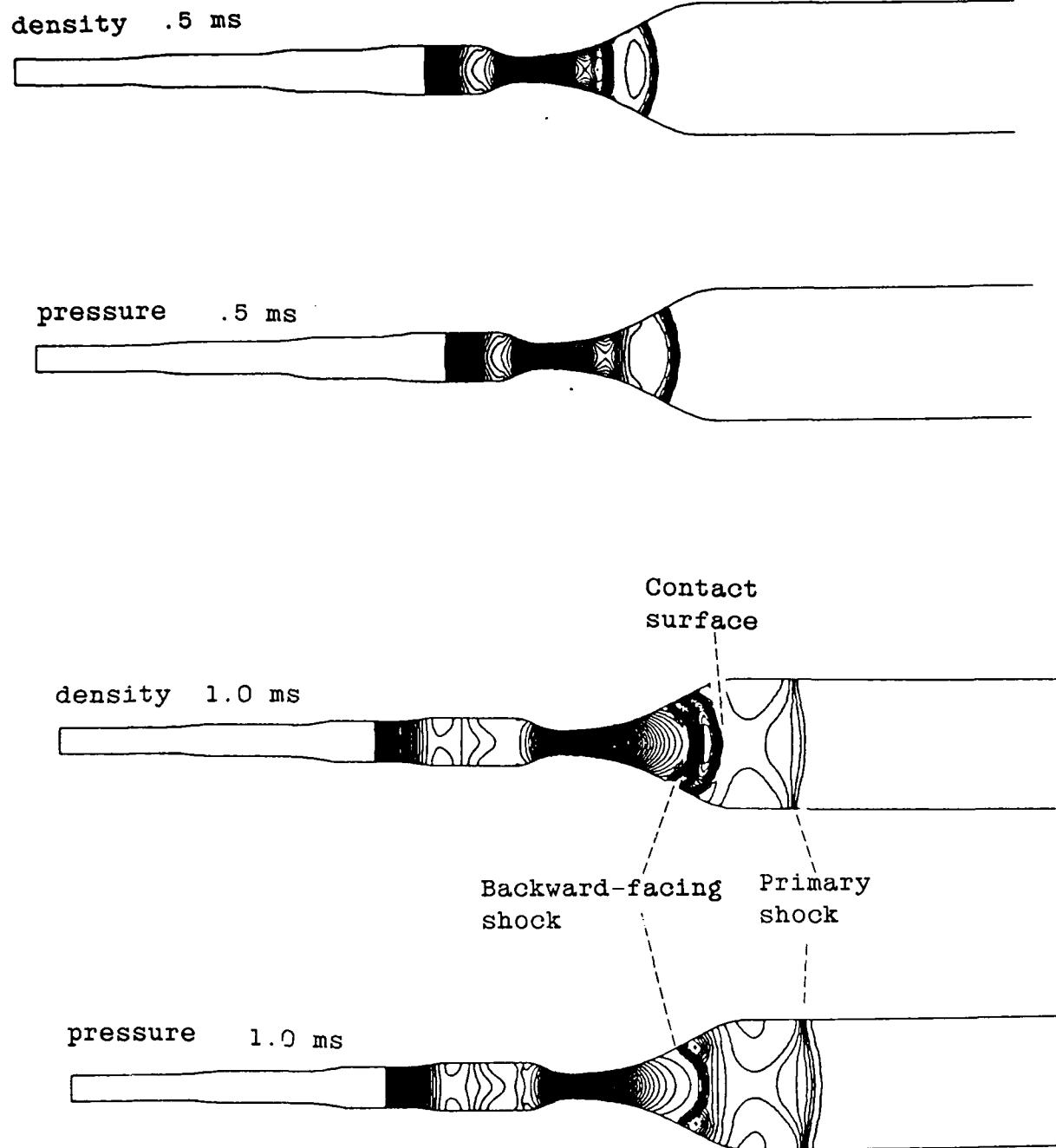
pressure   1.0 ms

Figure 6:   Contour Plots at .5 ms and 1.0 ms,
   34 kPa (5 psi) Peak Overpressure, Shot #2

26

Contour plot figure showing density and pressure at 1.4 ms and 1.9 ms, with labels for Contact surface, Backward-facing shock, and Primary shock.

density   1.4 ms

pressure   1.4 ms

Contact surface

Backward-facing shock

Primary shock

density   1.9 ms

pressure   1.9 ms

Contact surface

Backward-facing shock
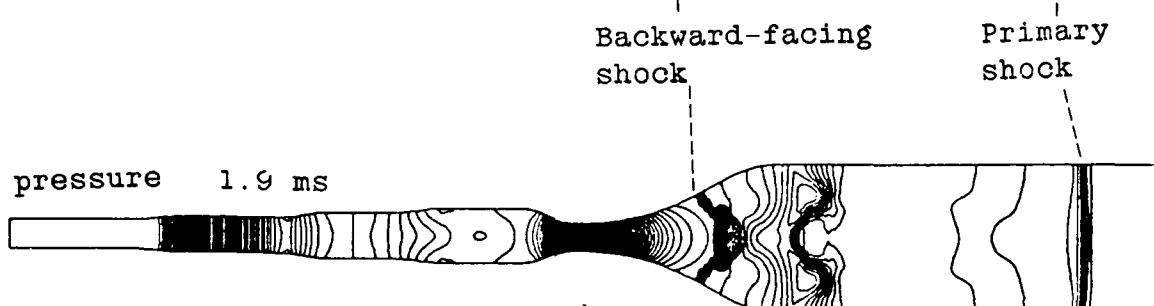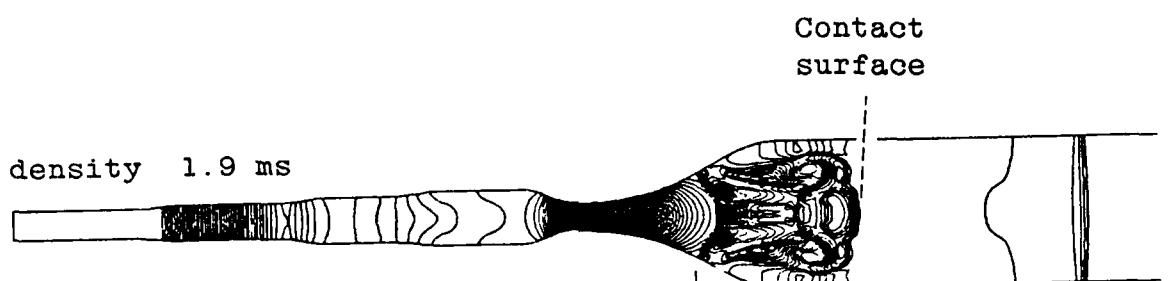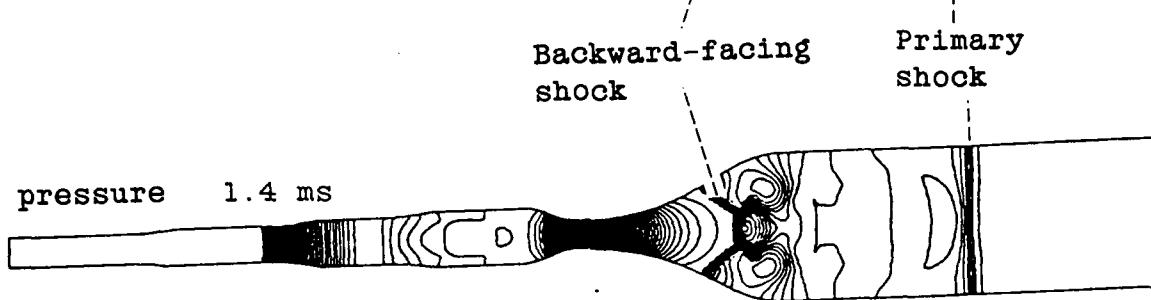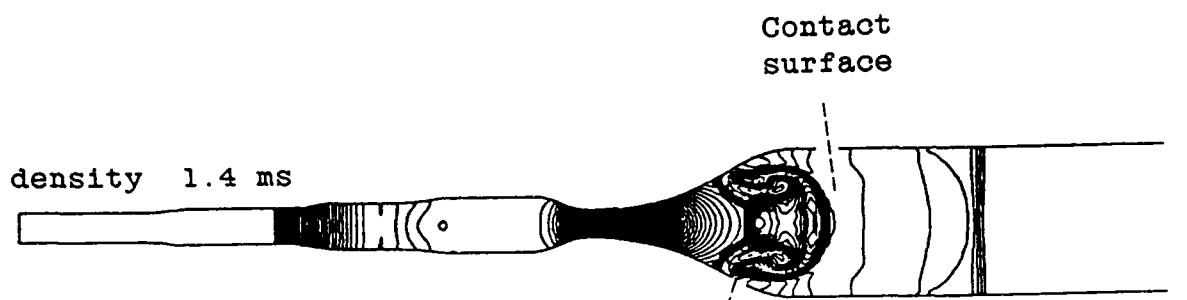
Primary shock

Figure 7:   Contour Plots at 1.4 ms and 1.9 ms,
            34 kPa (5 psi) Peak Overpressure, Shot #2

27

density   5.4 ms   Contact
                        surface

Backward-facing
shock

pressure   5.4 ms

                        Contact
                        surface
density   23.0 ms

Backward-facing
shock

pressure   23.0 ms

Rotational
flow
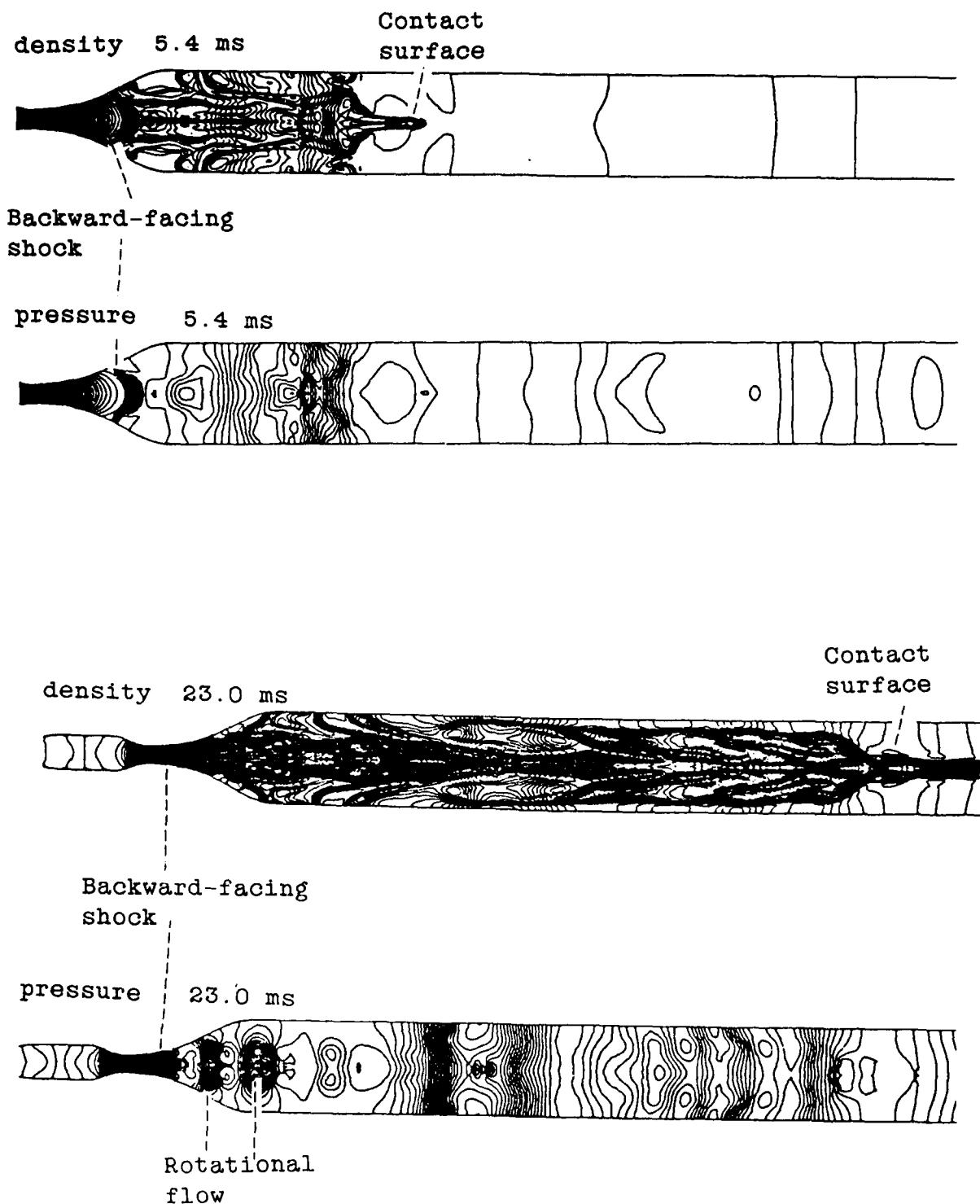
Figure 8:   Contour Plots at 5.4 ms and 23.0 ms,
            34 kPa (5 psi) Peak Overpressure, Shot #2

28
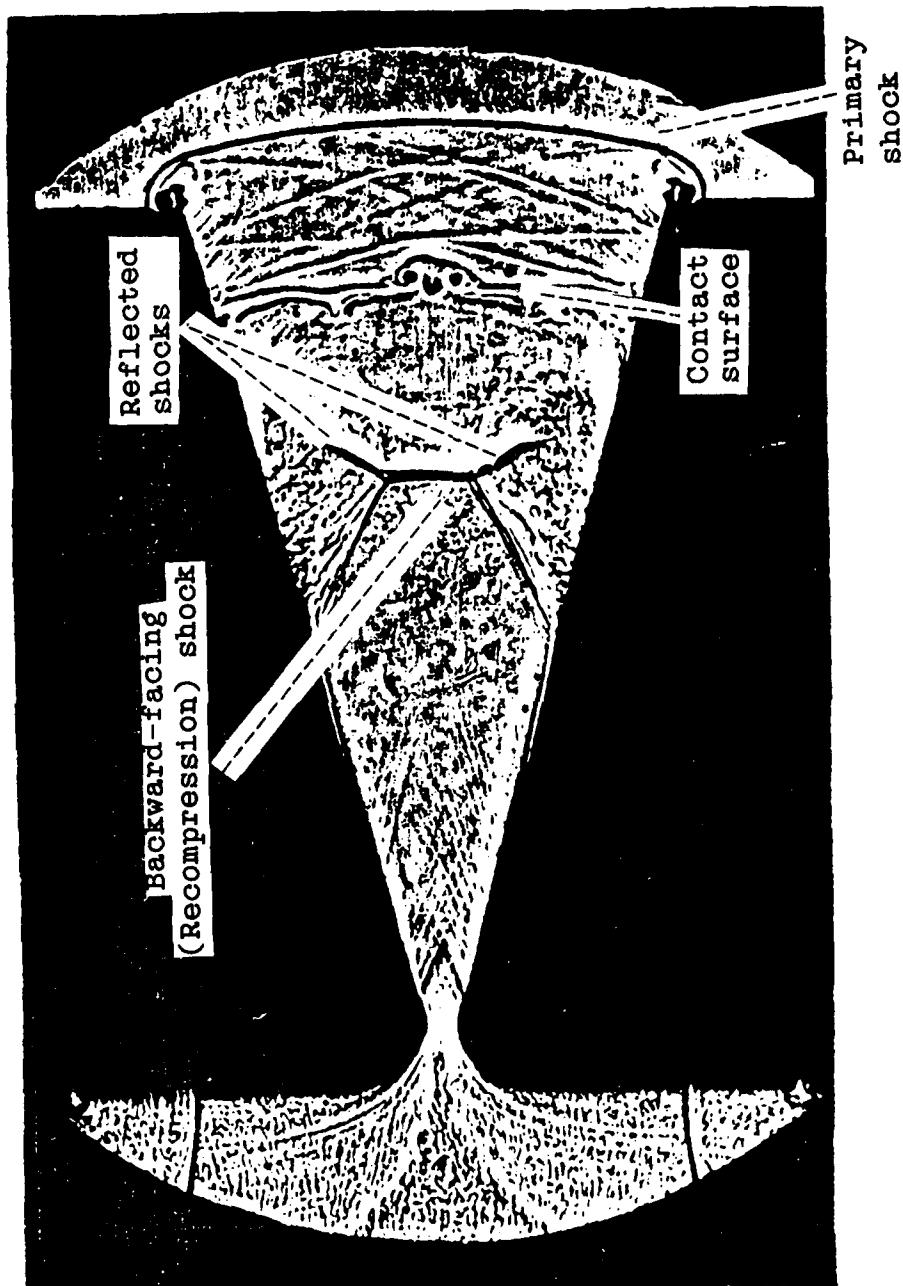
Figure 9: Development of Primary Shock, Contact, and Backward-facing Shock in Diverging Nozzle, Amann(8)
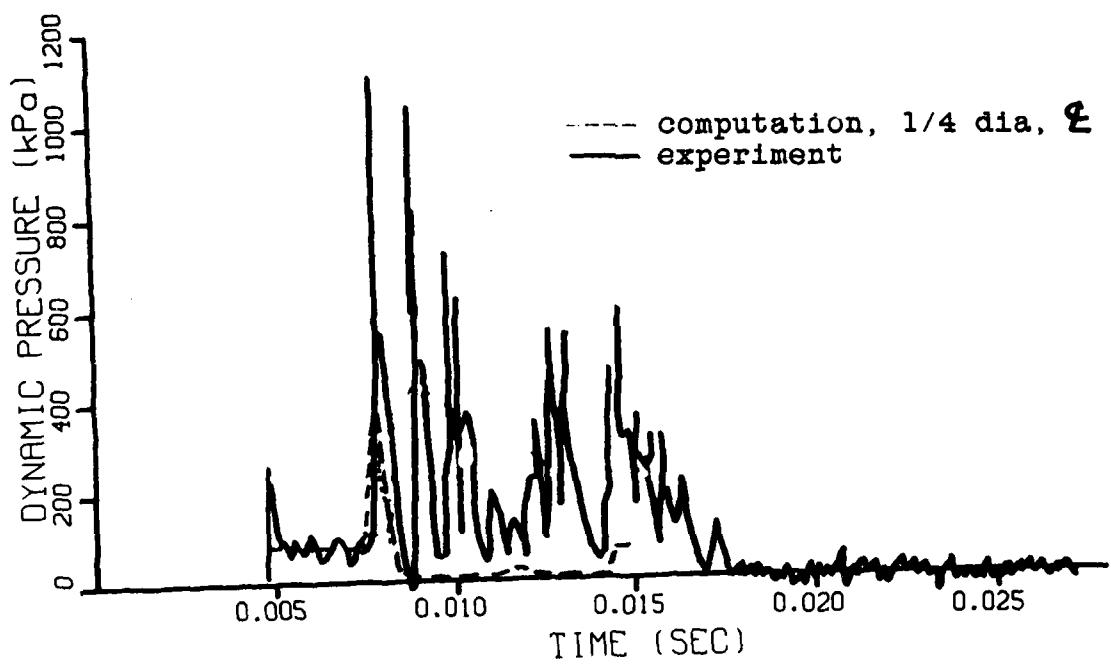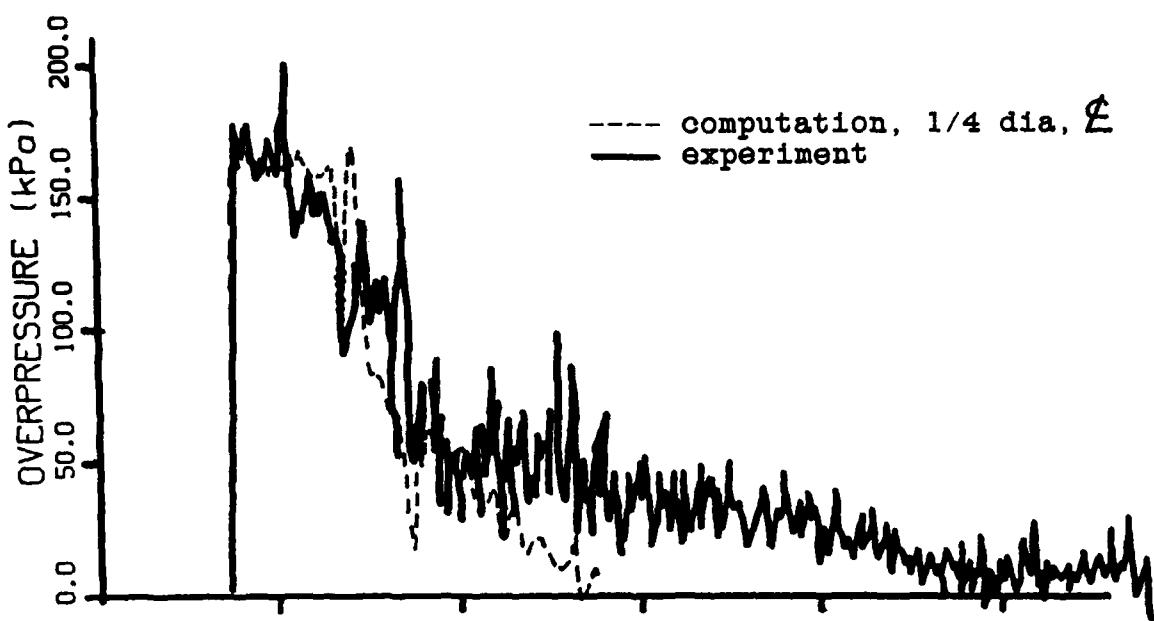
Figure 10: Pressure versus Time Plots, 175 kPa (25 psi)
Peak Overpressure, Unheated Driver, Shot #12

30
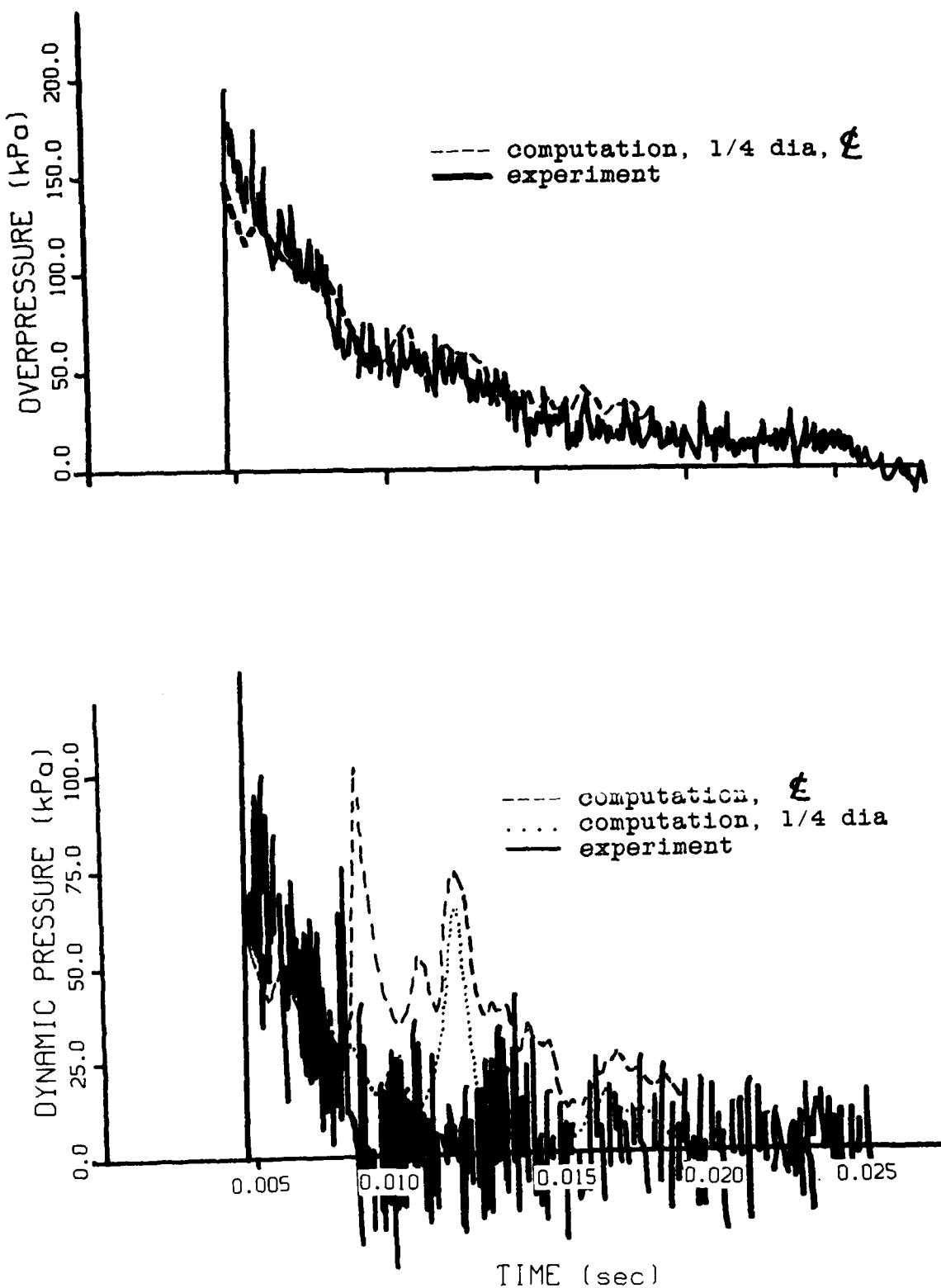
Figure 11: Pressure versus Time Plots, 175 kPa (25 psi)
Peak Overpressure, Heated Driver, Shot #85-11
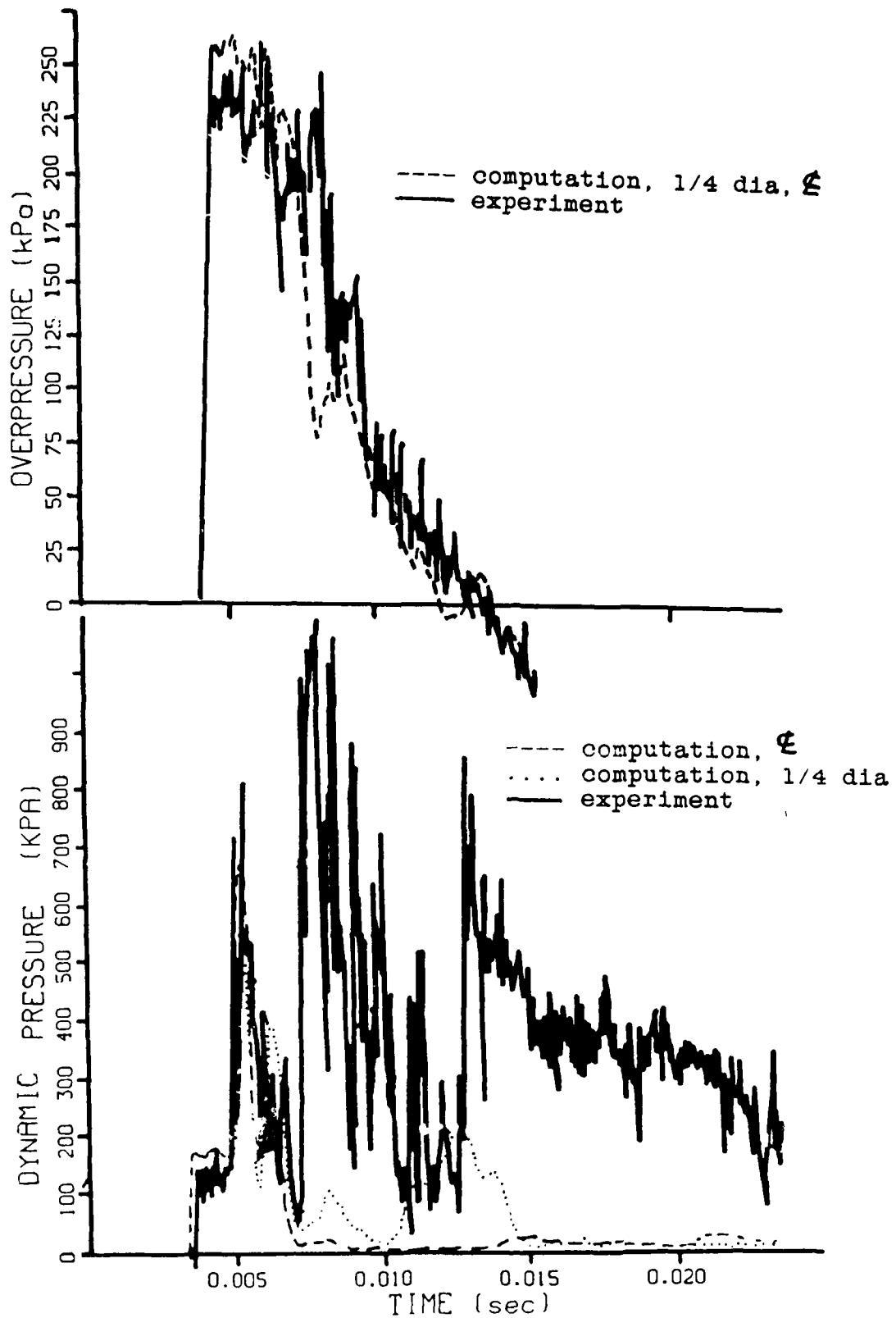
Figure 12: Pressure versus Time Plots, 245 kPa (35 psi)
Peak Overpressure, Unheated Driver, Shot #85-21
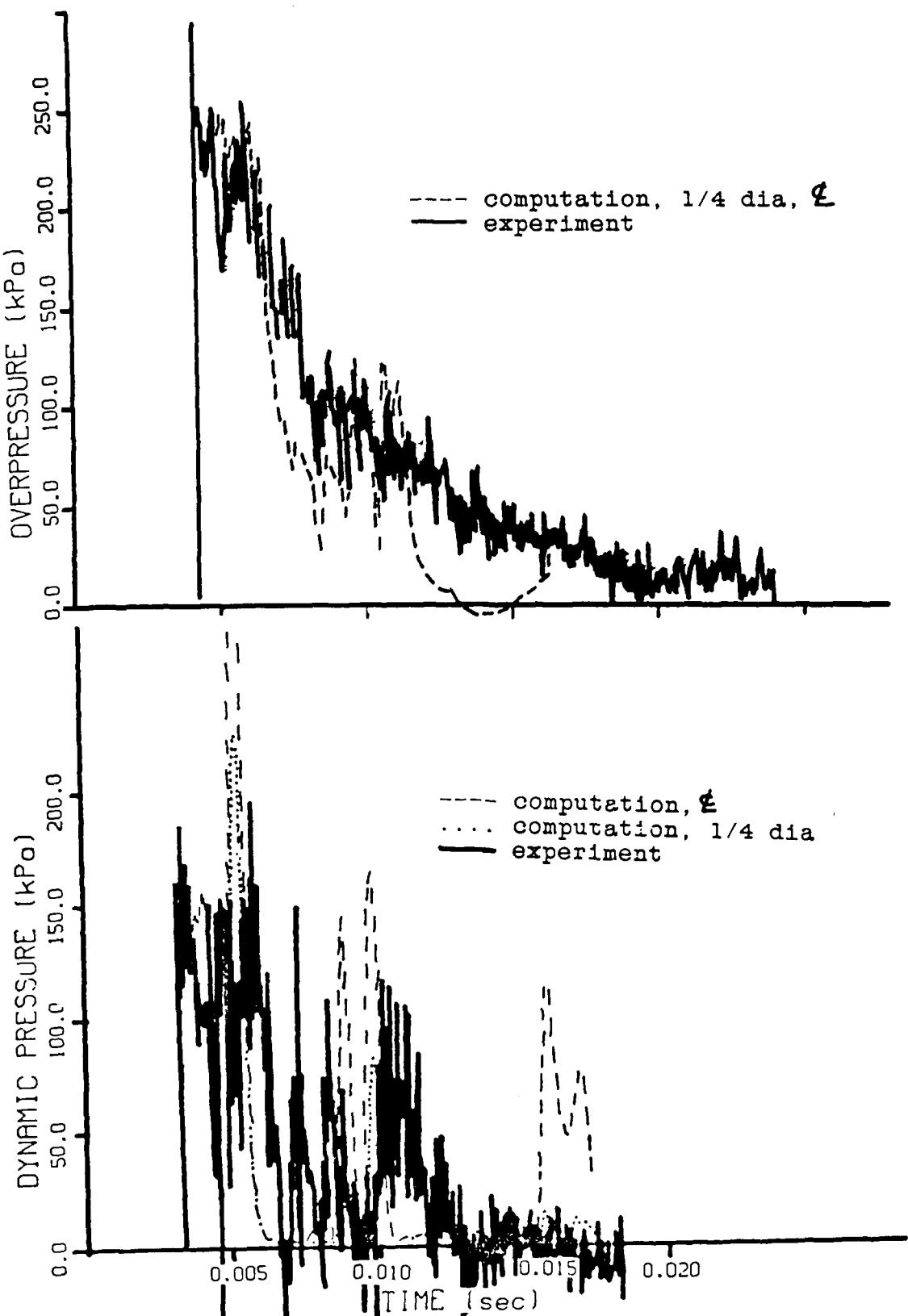
Figure 13: Pressure versus Time Plots, 245 kPa (35 psi)
Peak Overpressure, Heated Driver, Shot #85-23

density   .5 ms
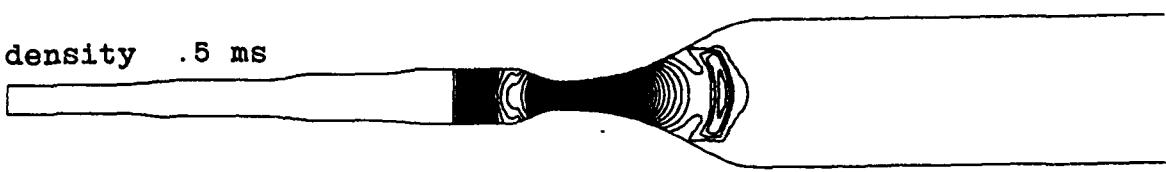
pressure   .5 ms
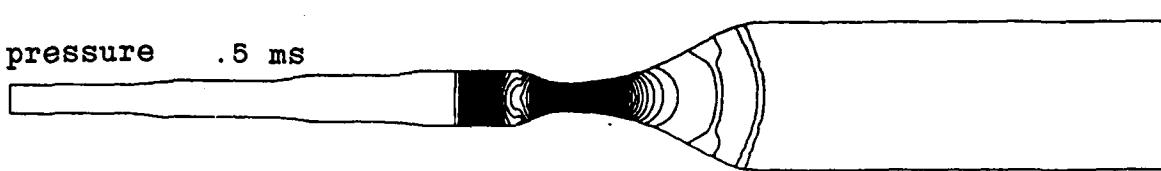
density   1.0 ms
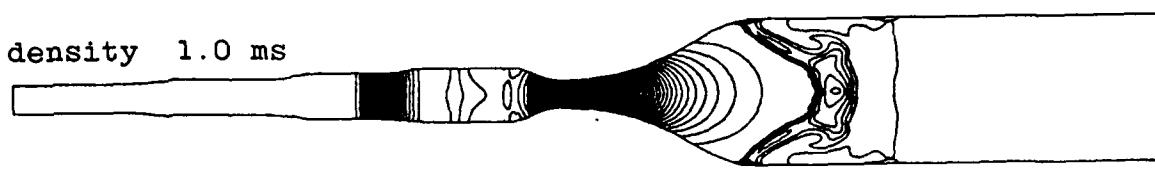
pressure   1.0 ms
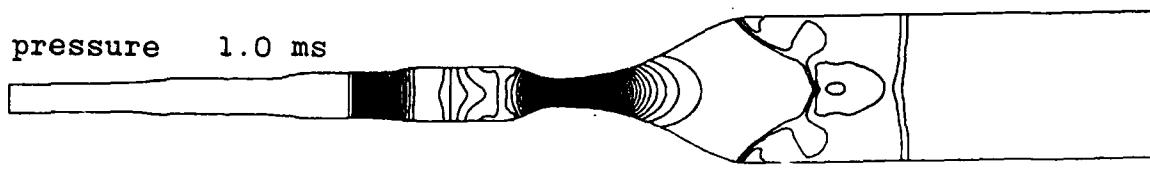
Figure 14:   Contour Plots at .5 ms and 1.0 ms,
              241 kPa (35 psi) Peak Overpressure,
   Shot #85-21, Unheated Driver

density   1.5 ms

pressure   1.5 ms

density   2.0 ms
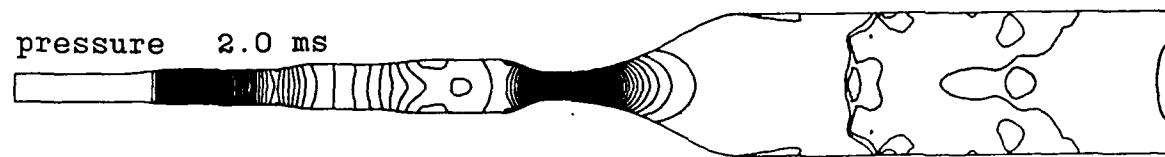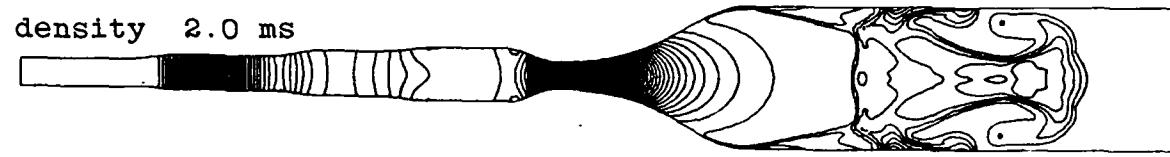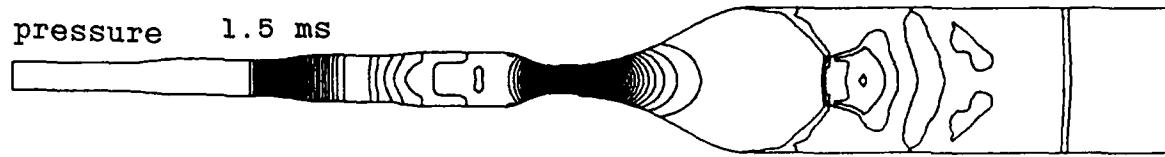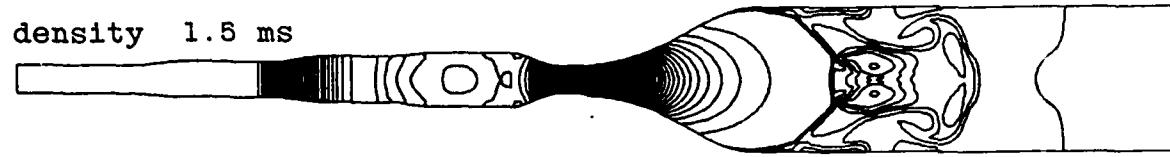
pressure   2.0 ms

Figure 15:   Contour Plots at 1.5 ms and 2.0 ms,
             241 kPa (35 psi) Peak Overpressure,
             Shot #85-21, Unheated Driver

35

density   5.6 ms

pressure   5.6 ms

density   23.4 ms
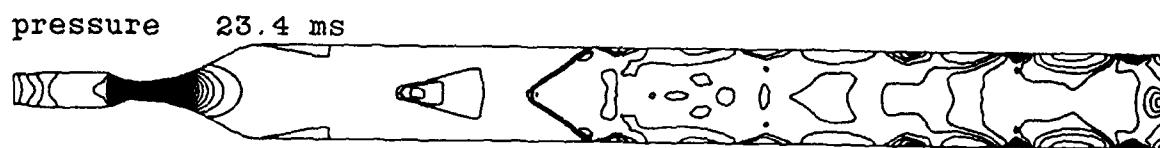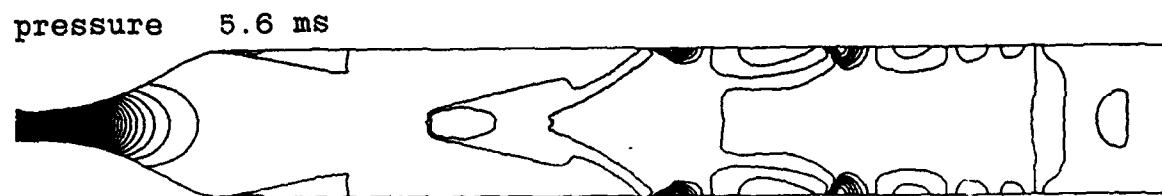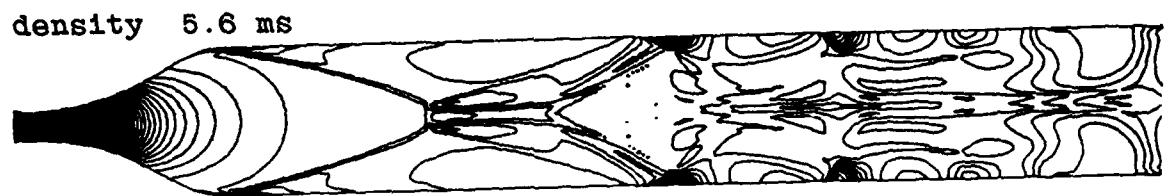
pressure   23.4 ms

Figure 16:   Contour Plots at 5.6 ms and 23.4 ms,
             241 kPa (35 psi) Peak Overpressure,
             Shot #85-21, Unheated Driver

density   .4 ms
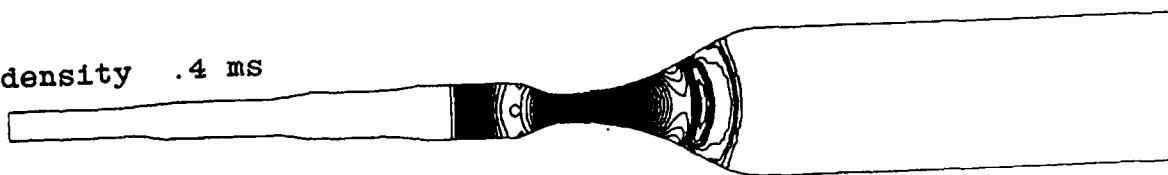
pressure   .4 ms
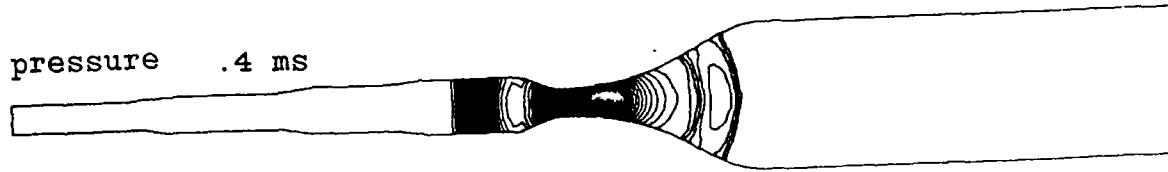
density   .7 ms
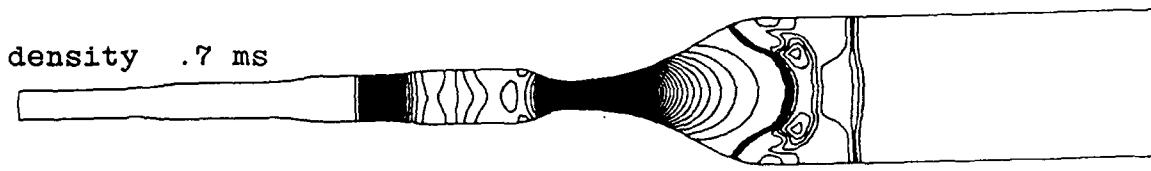
pressure   .7 ms
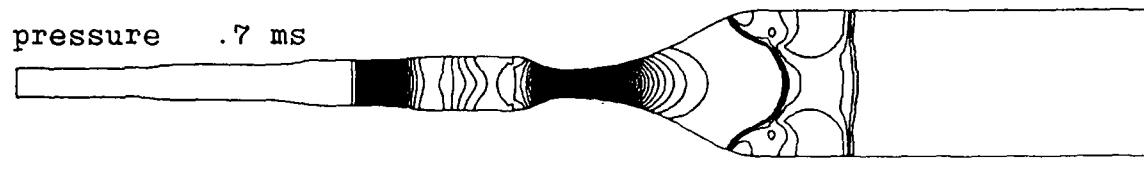
Figure 17:   Contour Plots at .4 ms and .7 ms,
             241 kPa (35 psi) Peak Overpressure,
             Shot #85-23, Heated Driver

density   1.1 ms

pressure   1.1 ms

density   1.5 ms
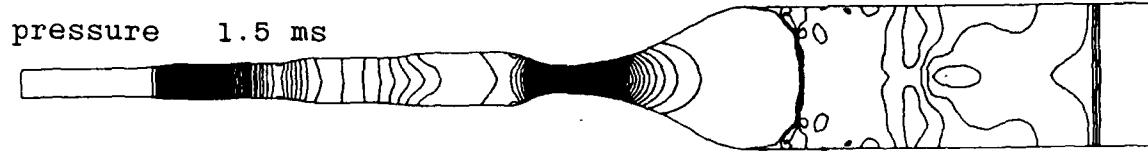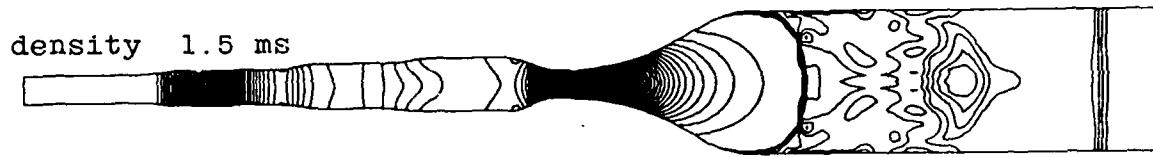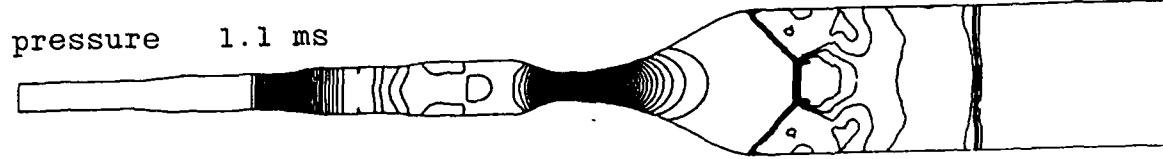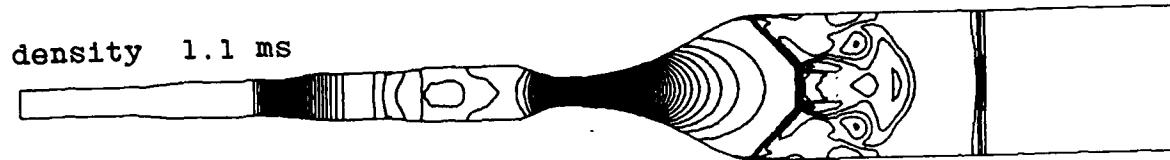
pressure   1.5 ms

Figure 18:   Contour Plots at 1.1 ms and 1.5 ms,
             241 kPa (35 psi) Peak Overpressure,
             Shot #85-23, Heated Driver

38

density   4.1 ms

pressure   4.1 ms

density   17.3 ms
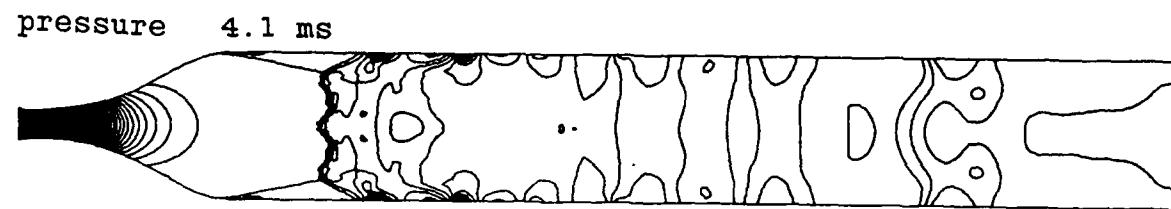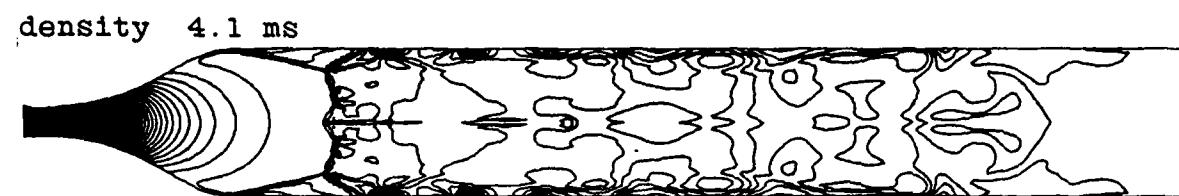
pressure   17.3 ms

Figure 19:   Contour Plots at 4.1 ms and 17.3 ms,
             241 kPa (35 psi) Peak Overpressure,
             Shot #85-23, Heated Driver

DISTRIBUTION LIST

No. of Copies	Organization	No. of Copies	Organization

12	Administrator
	Defense Technical Information
	  Center
	ATTN: DTIC-FDAC
	Cameron Station, Bldg 5
	Alexandria, VA 22304-6145
		9	Director
			Defense Nuclear Agency
			ATTN: DDST
			      TIPL/Tech Lib
			      SPSS/K. Goering
			      SPTD/T. Kennedy
			      SPAS/P.R. Rohr
			           G. Ullrich
			      STSP/COL Kovel
			      NATD
			      NATA
			Washington, DC 20305

1	Director of Defense Research & Engineering ATTN: DD/TWP Washington, DC 20301		

1	Asst. to the Secretary of
	  Defense (Atomic Energy)
	ATTN: Document Control
	Washington, DC 20301
		2	Commander
			Field Command
			Defense Nuclear Agency
			ATTN: FCPR
			      FCTMOF

1	Director Defense Advanced Research Projects Agency ATTN: Tech Lib 1400 Wilson Boulevard Arlington, VA 22209		Kirtland AFB, NM 87115
		1	Commander Field Command, DNA Livermore Branch ATTN: FCPRL P.O. Box 808 Livermore, CA 94550

2	Director
	Federal Emergency Management
	  Agency
	ATTN: D. A. Bettge
	      Technical Library
	Washington, DC 20472
		1	HQDA (DAMA-ART-M)
			Washington, DC 20310

1	Director Defense Intelligence Agency ATTN: DT-2/Wpns & Sys Div Washington, DC 20301	10	C.I.A. OIR/DB/Standard GE47 HQ Washington, D.C. 20505
1	Director National Security Agency ATTN: E. F. Butala, R15 Ft. George G. Meade, MD 20755	1	Program Manager US Army BMD Program Office ATTN: John Shea 5001 Eisenhower Avenue Alexandria, VA 22333

1	Director
	Joint Strategic Target
	  Planning Staff JCS
	Offut AFB
	Omaha, NB 68113
		2	Commander
			US Army BMD Advanced
			  Technology Center
			ATTN: CRDABH-X
			      CRDABH-S
			P.O. Box 1500
			Huntsville, AL 35807

DISTRIBUTION LIST

No. of Copies	Organization
1	Commander US Army BMD Command ATTN: BDMSC-TFN/N.J. Hurst P.O. Box 1500 Huntsville, AL 35807
1	Commander US Army Engineer Division ATTN: HNDED-FD P.O. Box 1500 Huntsville, AL 35807
2	Deputy Chief of Staff for Operations and Plans ATTN: Technical Library Director of Chemical & Nuc Operations Department of the Army Washington, DC 20310
3	Director US Army Engineer Waterways Experiment Station ATTN: Technical Library Jim Watt Jim Ingram P.O. Box 631 Vicksburg, MS 39180-0631
1	Commander US Army Materiel Command ATTN: AMCDRA-ST 5001 Eisenhower Avenue Alexandria, VA 22333-0001
1	Commander US Army Armament Research, Development and Engineering Center ATTN: SMCAR-MSI Dover, NJ 07801-5001
1	Commander US Army Armament Research, Development and Engineering Center ATTN: SMCAR-TDC Dover, NJ 07801

No. of Copies	Organization
1	U.S. Army Armament, Munitions and Chemical Command ATTN: AMSMC-IMP-L Rock Island, IL 61299-7300
1	Commander US AMCCOM ARDEC CCAC Benet Weapons Laboratory ATTN: SMCAR-CCB-TL Watervliet, NY 12189-4050
1	Commander U.S. Army Aviation Systems Command ATTN: AMSAV-ES 4300 Goodfellow Blvd. St. Louis, MO 63120-1798
1	Director U.S. Army Aviation Research and Technology Activity Ames Research Center Moffett Field, CA 94035-1099
1	Commander US Army Communications - Electronics Command ATTN: AMSEL-ED Fort Monmouth, NJ 07703-5301
1	Commander US Army Communications Rsch and Development Command ATTN: DRSEL-ATDD Fort Monmouth, NJ 07703
1	Commander CECOM R&D Technical Library ATTN: AMSEL-IM-L (Reports Section) B.2700 Fort Monmouth, NJ 07703-5301
2	Commander US Army Electronics Research and Development Command ATTN: DELEW-E, W. S. McAfee DELSD-EI, J. Roma Fort Monmouth, NJ 07703-5301

DISTRIBUTION LIST

No. of Copies	Organization	No. of Copies	Organization

6	Director
	US Army Harry Diamond Labs
	ATTN: Mr. James Gaul
	    Mr. L. Belliveau
	    Mr. J. Meszaros
	    Mr. J. Gwaltney
	    Mr. Bill Vault
	    Mr. R. J. Bostak
	2800 Powder Mill Road
	Adelphi, MD 20783-1197
		1	Commander
			US Army Logistics Management
			    Center
			ATTN: ATCL-O,
			        Mr. Robert Cameron
			Fort Lee, VA 23801

4	Director
	US Army Harry Diamond Labs
	ATTN: SLCHD-TA-L
	    DRXDO-TI/002
	    DRXDO-NP
	    SLCHD-RBA/J. Rosado
	2800 Powder Mill Road
	Adelphi, MD 20783-1197
		2	Commander
			US Army Materials Technology
			    Laboratory
			ATTN: AMXMR-ATL
			        Eugene de Luca
			Watertown, MA 02172-0001

1	Commander US Army Missile Command ATTN: AMSMI-RD Redstone Arsenal, AL 35898-5245	1	Commander US Army Research Office ATTN: SLCRO-D P.O. Box 12211 Research Triangle Park NC 27709-2211

1	Director
	US Army Missile and Space
	    Intelligence Center
	ATTN: AIAMS-YDL
	Redstone Arsenal, AL 35898-5500
		4	Commander
			US Army Nuclear & Chemical
			    Agency
			ATTN: ACTA-NAW
			        MONA-WE
			        Technical Library
			        LTC Finno
			7500 Backlick Rd, Bldg. 2073
			Springfield, VA 22150

2	Commander
	US Army Natick Research and
	    Development Center
	ATTN: AMDNA-D/Dr. D. Sieling
	        STRNC-UE/J. Calligeros
	Natick, MA 01762
		1	Commander
			US Army TRADOC
			ATTN: DCST&E
			Fort Monroe, VA 23651

1	Commander
	US Army Tank-Automotive Command
	ATTN: AMSTA-TSL
	Warren, MI 48397-5000
		2	Director
			US Army TRADOC Systems
			    Analysis Activity
			ATTN: LTC John Hesse
			        ATOR-TSL
			White Sands Missile Range, NM
			    88002-5502

1	Commander US Army Foreign Science and Technology Center ATTN: Research and Data Br 220 7th Street , NE Charlottesville, VA 22901	2	Commandant U.S. Army Infantry School ATTN: ATSH-CD-CS-OR Fort Benning, GA 31905-5400

DISTRIBUTION LIST

No. of Copies	Organization	No. of Copies	Organization

1	Commander
	U.S. Army Development and
	  Employment
	  Agency
	ATTN: MODE-ORO
	Fort Lewis, WA 98433-5000
		1	Commander
			Naval Sea Systems Command
			ATTN: Code SEA-62R
			Department of the Navy
			Washington, DC 20362-5101

1	Commandant
	Interservice Nuclear Weapons
	  School
	ATTN: Technical Library
	Kirtland AFB, NM 87115
		3	Officer-in-Charge(Code L31)
			Civil Engineering Laboratory
			Naval Construction Battalion
			  Center
			ATTN: Stan Takahashi
			      R. J. Odello
			      Technical Library
			Port Hueneme, CA 93041

1	Chief of Naval Material ATTN: MAT 0323 Department of the Navy Arlington, VA 22217	1	Commander David W. Taylor Naval Ship Research & Development Command ATTN: Lib Div, Code 522 Bethesda, MD 20084-5000
2	Chief of Naval Operations ATTN: OP-03EG OP-985F Department of the Navy Washington, DC 20350	1	Commander Naval Surface Weapons Center ATTN: DX-21, Library Br. Dahlgren, VA 22448-5000

1	Chief of Naval Research
	ATTN: N. Perrone
	Department of the Navy
	Arlington, VA 22217
		2	Commander
			Naval Surface Weapons Center
			ATTN: Code WA501/Navy Nuclear
			           Programs Office
			      Code WX21/Tech Library

1	Director Strategic Systems Projects Ofc ATTN: NSP-43, Tech Library Department of the Navy Washington, DC 20360		Silver Spring, MD 20902-5000
1	Commander Naval Electronic Systems Com ATTN: PME 117-21A Washington, DC 20360	1	Commander Naval Weapons Center ATTN: Code 533, Tech Lib China Lake, CA 93555-6001
1	Commander Naval Facilities Engineering Command Washington, DC 20360	1	Commander Naval Weapons Evaluation Fac ATTN: Document Control Kirtland AFB, NM 87117
		1	Commander Naval Research Laboratory ATTN: Code 2027, Tech Lib Washington, DC 20375

DISTRIBUTION LIST

DISTRIBUTION LIST

No. of Copies	Organization	No. of Copies	Organization

3   Aberdeen Research Center
ATTN: N.H. Ethridge
      J. Keefer
      Library
P.O. Box 548
30 Diamond Street
Aberdeen, MD 21001

1   Aerospace Corporation
ATTN: Tech Info Services
P.O. Box 92957
Los Angeles, CA 90009

1   Agbabian Associates
ATTN: M. Agbabian
250 North Nash Street
El Segundo, CA 90245

1   The BDM Corporation
ATTN: Richard Hensley
P.O. Box 9274
Albuquerque International
Albuquerque, NM 87119

1   The Boeing Company
ATTN: Aerospace Library
P.O. Box 3707
Seattle, WA 98124

1   California Research
    and Technology
ATTN: F. Sauer
Suite B 130
11875 Dublin Blvd
Dublin, CA 94568

1   California Research & Technology,
    Inc.
ATTN: M. Rosenblatt
20943 Devonshire Street
Chatsworth, CA 91311

1   Carpenter Research Corporation
ATTN: H. Jerry Carpenter
Suite 424
904 Silver Spur Road
Rolling Hills Estates, CA 90274

1   Goodyear Aerospace Corp
ATTN: R. M. Brown, Bldg 1
      Shelter Engineering
Litchfield Park, AZ 85340

6   Kaman AviDyne
ATTN: Dr. R. Reutenick
      (4 cys)
      Mr. S. Criscione
      Mr. R. Milligan
83 Second Avenue
Northwest Industrial Park
Burlington, MA 01830

3   Kaman Sciences Corporation
ATTN: Library
      P. A. Ellis
      F. H. Shelton
1500 Garden of the Gods Road
Colorado Springs, CO 80907

2   Kaman-TEMPO
ATTN: DASIAC
      Don Sachs
P.O. Drawer QQ
816 State Street
Santa Barbara, CA 93102

1   Lockheed Missiles & Space Co.
ATTN: J. J. Murphy, Dept.
      81-11, Bldg. 154
P.O. Box 504
Sunnyvale, CA 94086

1   Martin Marietta Aerospace
Orlando Division
ATTN: G. Fotieo
P.O. Box 5837
Orlando, FL 32805

2   McDonnell Douglas Astronautics
    Corporation
ATTN: Robert W. Halprin
      K.A. Heinly
5301 Bolsa Avenue
Huntington Beach, CA 92647

DISTRIBUTION LIST

No. of Copies	Organization	No. of Copies	Organization
1	New Mexico Engineering Research Institute (CERF) ATTN: J. Leigh P.O. Box 25 UNM Albuquerque, NM 87131	1	Texas Engineering Experiment Station ATTN: Dr. D. Anderson 301 Engineering Research Center College Station, TX 77843
2	Physics International Corp 2700 Merced Street San Leandro, CA 94577	2	TRW Systems Group ATTN: Benjamin Sussholtz Stanton Fink One Space Park Redondo Beach, CA 90278
2	R&D Associates ATTN: Technical Library Allan Kuhl P.O. Box 9695 Marina del Rey, CA 90291	1	Battelle Memorial Institute ATTN: Technical Library 505 King Avenue Columbus, OH 43201
1	R&D Associates ATTN: G.P. Ganong P.O. Box 9335 Albuquerque, NM 87119	1	California Inst of Tech ATTN: T. J. Ahrens 1201 E. California Blvd. Pasadena, CA 91109
2	Science Applications, Inc. ATTN: W. Layson John Cockayne PO BOX 1303 1710 Goodridge Drive McLean, VA 22102	2	Denver Research Institute University of Denver ATTN: Mr. J. Wisotski Technical Library PO Box 10127 Denver, CO 80210
1	Science Applications, Inc. ATTN: Technical Library 1250 Prospect Plaza La Jolla, CA 92037	1	TRW Ballistic Missile Division ATTN: H. Korman, Mail Station 526/614 P.O. Box 1310 San Bernadino, CA 92402
2	Systems, Science and Software ATTN: C. E. Needham Lynn Kennedy PO Box 8243 Albuquerque, NM 87198	1	Massachusetts Institute of Technology Aeroelastic and Structures Research Laboratory ATTN: Dr. E. A. Witmer Cambridge, MA 02139
3	Systems, Science and Software ATTN: Technical Library R. Duff K. Pyatt PO Box 1620 La Jolla, CA 92037	2	Southwest Research Institute ATTN: Dr. W. E. Baker A. B. Wenzel 8500 Culebra Road San Antonio, TX 78228

47

DISTRIBUTION LIST

No. of
Copies   Organization

1   SRI International
     ATTN: Dr. G. R.
           Abrahamson
     333 Ravenswood Avenue
     Menlo Park, CA 94025

1   Stanford University
     ATTN: Dr. D. Bershader
     Durand Laboratory
     Stanford, CA 94305

Aberdeen Proving Ground

    Dir, USAMSAA
       ATTN: AMXSY-D
            AMXSY-MP, H. Cohen
    Cdr, USATECOM
       ATTN: AMSTE-SI-F
    Cdr, CRDC, AMCCOM
       ATTN: SMCCR-RSP-A
            SMCCR-MU
            SMCCR-SPS-IL

USER EVALUATION SHEET/CHANGE OF ADDRESS

This Laboratory undertakes a continuing effort to improve the quality of the reports it publishes. Your comments/answers to the items/questions below will aid us in our efforts.

1. BRL Report Number_____ Date of Report_____

2. Date Report Received_____

3. Does this report satisfy a need? (Comment on purpose, related project, or other area of interest for which the report will be used.)_____

_____

_____

4. How specifically, is the report being used? (Information source, design data, procedure, source of ideas, etc.)_____

_____

_____

5. Has the information in this report led to any quantitative savings as far as man-hours or dollars saved, operating costs avoided or efficiencies achieved, etc? If so, please elaborate._____

_____

_____

6. *General Comments. What do you think should be changed to improve future reports?* (Indicate changes to organization, technical content, format, etc.)

_____

_____

_____

	Name_____
CURRENT ADDRESS	Organization_____
	Address_____
	City, State, Zip_____

7. If indicating a Change of Address or Address Correction, please provide the New or Correct Address in Block 6 above and the Old or Incorrect address below.

	Name_____
OLD ADDRESS	Organization_____
	Address_____
	City, State, Zip_____

(Remove this sheet, fold as indicated, staple or tape closed, and mail.)